

MRI2Qmap: multi-parametric quantitative mapping with MRI-driven denoising priors

Mohammad Golbabaee, Matteo Cencini, Carolin Pirkl, Marion Menzel, Michela Tosetti, and Bjoern Menze

Abstract—Magnetic Resonance Fingerprinting (MRF) and other highly accelerated transient-state parameter mapping techniques enable simultaneous quantification of multiple tissue properties, but often suffer from aliasing artifacts due to compressed sampling. Incorporating spatial image priors can mitigate these artifacts, and deep learning has shown strong potential when large training datasets are available. However, extending this paradigm to MRF-type sequences remains challenging due to the scarcity of quantitative imaging data for training. *Can this limitation be overcome by leveraging sources of training data from clinically-routine weighted MRI images?* To this end, we introduce MRI2Qmap, a plug-and-play quantitative reconstruction framework that integrates the physical acquisition model with priors learned from deep denoising autoencoders pretrained on large multimodal weighted-MRI datasets. MRI2Qmap demonstrates that spatial-domain structural priors learned from independently acquired datasets of routine weighted-MRI images can be effectively used for quantitative MRI reconstruction. The proposed method is validated on highly accelerated 3D whole-brain MRF data from both *in-vivo* and simulated acquisitions, achieving competitive or superior performance relative to existing baselines without requiring ground-truth quantitative imaging data for training. By decoupling quantitative reconstruction from the need for ground-truth MRF training data, this framework points toward a scalable paradigm for quantitative MRI that can capitalize on the large and growing repositories of routine clinical MRI.

Index Terms—Quantitative MRI, compressed sampling, image reconstruction, deep learning.

I. INTRODUCTION

Quantitative MRI (qMRI) enables measurement of tissue biophysical parameters, such as T1 and T2 relaxation times, and provides objective imaging biomarkers for tissue characterization and disease monitoring [1]. However, conventional qMRI is bottlenecked by long acquisition times, as multiple image series must be acquired and repeated for each parameter, making clinical adoptions challenging. Magnetic Resonance Fingerprinting (MRF) [2] and related transient-state methods [3]–[5] address this limitation by jointly encoding multiple tissue parameters using short dynamically-varying excitation sequences and highly undersampled k-space acquisitions. While substantially reducing scan time, such acceleration can introduce pronounced aliasing artifacts, necessitating advanced algorithms to mitigate them for accurate quantitative mapping.

Methods for MRF reconstruction range from variational formulations that combine physical acquisition constraints with classical sparsity and low-rank image priors [6]–[8],

to more recent deep learning approaches that leverage data-driven priors and the strong representational capacity of neural networks, which now define the state of the art [9]–[12]. Most existing methods rely on supervised, end-to-end training to map undersampled MRF data to high-quality, densely sampled quantitative maps. Their performance, however, critically depends on large training datasets with paired ground-truth parameter maps, which are difficult—if not impractical—to obtain due to prohibitively long scan times. Moreover, unlike conventional weighted MRI, qMRI acquisitions (accelerated or not) are not yet a clinical routine, resulting in limited dataset size and diversity. Reducing this reliance on quantitative training data therefore remains a central challenge.

Given the far broader availability of routine weighted-MRI data compared with quantitative MRI, and the structural overlap between these imaging domains, we ask whether MRF reconstruction can benefit from priors learned from independently acquired weighted-MRI datasets. These imaging domains are related: multi-parametric quantitative maps, including those estimated by MRF, can be used to synthesize conventional weighted-MRI contrasts across multiple modalities via Bloch equations [4], [13], [14]. Building on this connection, we propose MRI2Qmap, a plug-and-play framework that integrates spatial priors learned from multimodal weighted-MRI datasets into MRF reconstruction from undersampled acquisitions. MRI2Qmap comprises three key components: (i) Bloch signal models to synthesize multiple weighted-MRI contrasts from estimated quantitative maps; (ii) restoration of these synthesized images using deep denoising autoencoders pretrained on large weighted-MRI datasets; and (iii) iterative updates of the quantitative maps that enforce joint consistency with the scan-specific physical acquisition model, measured data, and the spatially-restored synthesized images provided by the denoising priors. Our experiments on highly accelerated 3D whole-brain MRF acquisitions demonstrate that MRI-driven priors are effective in mitigating undersampling artifacts while capable of producing high-quality quantitative maps.

A. Related works

1) *Model-based approaches*: Early MRF works [2], [15] employed Fourier back-projection to convert undersampled k-space data into image time-series, followed by dictionary matching, where voxels signal evolutions were compared to a dictionary of theoretical tissue fingerprints from Bloch equations, for quantitative mapping. Subsequent studies minimized a k-space loss while enforcing Bloch constraints through iterative dictionary matching [6], [16]. To reduce computational cost, approximate matching strategies [17], [18] and

MG is with University of Bristol (m.golbabaee@bristol.ac.uk). MC/MT are with IRCCS Fondazione Stella Maris. CP/MM are with GE Healthcare. MM is also with TH Ingolstadt. BM is with the University of Zurich.

low-rank subspace models for dictionary compression [6], [15], [19] were introduced. However, the absence of spatial regularization left these approaches prone to aliasing artifacts. Later works e.g. [5], [7], [8], [20], [21] included sparsity and low-rank regularization to reduce these artifacts; While effective, their performance usually lags behind deep learning methods, particularly at highly accelerated acquisitions.

2) *Deep learning approaches*: Early MRF deep learning works [22]–[24] used relatively small networks for voxel-wise parameter mapping after image reconstruction; however, by processing voxels independently, these approaches lacked the spatial context necessary to mitigate correlated aliasing artifacts. In contrast, dominant recent literature incorporates spatial information by training on anatomical MRF maps using various architectures including convolutional networks [9], [11], [25], [26], deep unrolling [10], [27], plug-and-play [28], transformers [29], and diffusion models [12]. Despite improved performance, these methods remain fundamentally constrained by the scarcity of MRF data and high-quality anatomical ground-truth, which limits their scalability. Some more recent studies also explored scan-specific (zero-shot) reconstructions, for the classical qMRI [30], multi-parametric imaging [31], and transient-state MRF [32], [33], using only undersampled k-space data from one subject for training. While mitigating the need for ground-truth, these methods incur substantial computational cost, requiring *de novo* network training for each scan, involving thousands of iterations for 2D reconstructions [30], [32], [33], and several GPU-hours for 3D Cartesian acquisitions [31] despite the lower computational burden of Cartesian imaging relative to non-Cartesian MRF. Moreover, prior work (e.g., [34]) suggests that effective reconstruction benefits from incorporating spatial-domain priors to compensate for information missing in highly undersampled measurements with large, non-trivial null spaces.

Our approach differs from the above paradigms by addressing quantitative data scarcity through priors learned from clinically ubiquitous, high-quality weighted MRI datasets, and by introducing an efficient algorithm that enables scan-specific, multicoil, 3D whole-brain non-Cartesian MRF reconstruction within minutes on a single GPU, without requiring qMRI/MRF training datasets or per-scan network retraining.

II. PRELIMINARIES

A. The MRF inverse problem

MRF reconstruction is a nonlinear inverse problem:

$$\mathbf{y} \approx \mathcal{A}(\mathbf{x}) \text{ such that } \mathbf{x}_v = \mathcal{B}^{\mathcal{Q}}(\mathbf{q}_v), \forall v : \text{voxels} \quad (1)$$

The goal is to estimate quantitative parameter maps (qmaps) $\mathbf{q} := \{\text{T1}, \text{T2}, \text{proton density (PD)}\}$ over n voxels. $\mathbf{x} \in \mathbb{C}^{s \times n}$ denotes the time series of magnetization images (TSMI) to be reconstructed. The nonlinear MRF Bloch response model voxel-wise encodes qmaps into s -dimensional signal evolutions (fingerprints) of the TSMI, scaled by proton density:

$$\mathbf{x}_v = \mathcal{B}^{\mathcal{Q}}(\mathbf{q}_v) := \text{PD}_v \cdot \text{BLOCH}^{\mathcal{Q}}(\text{T1}_v, \text{T2}_v) \quad (2)$$

The linear forward operator \mathcal{A} relates TSMI to the undersampled k-space measurements $\mathbf{y} \in \mathbb{C}^{l \times cm}$ from m spatial

frequency locations across c receiver coil channels, and l time frames. It includes coil sensitivity profiles, a nonuniform FFT, and a linear dimensionality reduction [6], [8], [15] which is commonly used for computationally efficient reconstructions by compressing the time dimension of TSMI into adequately smaller $s \ll l$ time frames (coefficient channels). Reconstruction further relies on an MRF *dictionary*, as a discretized approximation of (2), consisting of a lookup table (LUT) with d sampled T1–T2 combinations and their precomputed Bloch responses $D^{\mathcal{Q}} \in \mathbb{C}^{s \times d}$, where $D_j^{\mathcal{Q}} := \text{BLOCH}^{\mathcal{Q}}(j), \forall j \in \text{LUT}$. Projection of a TSMI $\tilde{\mathbf{x}}$ onto the Bloch constraint can be approximated by voxel-wise dictionary matching/search [16]:

$$\mathbf{q}_v^* \leftarrow \text{D-MATCH}(\tilde{\mathbf{x}}_v, D^{\mathcal{Q}}) \approx \underset{\mathbf{q}}{\text{argmin}} \|\tilde{\mathbf{x}}_v - \mathcal{B}^{\mathcal{Q}}(\mathbf{q})\|_2 \quad (3)$$

with $\text{D-MATCH}(\tilde{\mathbf{x}}_v, D^{\mathcal{Q}}) := \underset{\text{PD}, j \in \text{LUT}}{\text{arg min}} \|\tilde{\mathbf{x}}_v - \text{PD} \cdot D_j^{\mathcal{Q}}\|_2$.

B. Multimodal MRI synthesis

A key advantage of multi-parametric maps produced by MRF-type acquisitions is their ability to synthesize conventional weighted-MRI images across multiple contrast modalities [4], [13], [14]. Given quantitative maps $\mathbf{q} := \{\text{T1}, \text{T2}, \text{PD}\}$ common diagnostic contrasts (e.g., T1w, T2w, PDw) can be approximated via MRI Bloch signal models:

$$\mathcal{B}^{\mathcal{W}}(\mathbf{q}_v) := |\text{PD}_v| \cdot \text{BLOCH}^{\mathcal{W}}(\text{T1}_v, \text{T2}_v), \quad (4)$$

where $\mathcal{B}^{\mathcal{W}}$ denotes a voxel-wise mapping from qmaps to MRI magnitude images $\mathbf{m} \in \mathbb{R}^{s' \times n}$ across s' modalities. For example, under a spin-echo signal model with synthetic acquisition parameters repetition (TR) and echo (TE) times:

$$|\text{PD}_v| \exp(-\text{TE}/\text{T2}_v) (1 - \exp(-\text{TR}/\text{T1}_v)), \quad (5)$$

T1w contrast arises from short TE, T2w from long TR, and PDw from short TE combined with long TR. Importantly, these contrasts retain useful dependencies on the underlying quantitative properties. In this work, we exploit this cross-domain relationship by synthesizing weighted-MRI contrasts from intermediate quantitative estimates, enabling MRI-driven image priors to iteratively mitigate undersampling artifacts and improve quantitative reconstruction in accelerated MRF.

C. Reconstruction with Plug-and-Play denoising priors

Given image samples from an unknown data distribution p_x , a denoising autoencoder DAE(\cdot, σ^2) can be trained to remove additive Gaussian noise with variance σ^2 by minimizing

$$\mathbb{E}_{x \sim p_x, \epsilon \sim \mathcal{N}(0, \sigma^2 \mathbf{I})} \|\text{DAE}(x + \epsilon, \sigma^2) - x\|_2^2. \quad (6)$$

The resulting model implicitly captures useful surrogate priors about the underlying data distribution. The denoising residual $\text{DAE}(\tilde{x}, \sigma) - \tilde{x} \propto \nabla_{\tilde{x}} \log p_{x, \sigma}(\tilde{x})$ approximates the score (gradient of log-likelihood) of the data distribution smoothed by a Gaussian convolution $p_{x, \sigma} := p_x * \mathcal{N}(\mathbf{0}, \sigma^2 \mathbf{I})$ [35]. Thus, for sufficiently small σ , the DAE approximates a gradient-ascent step toward the manifold of plausible images. Denoising neural networks underpin modern plug-and-play (PnP) reconstruction methods [36]–[38], which embed pretrained denoisers into iterative optimization algorithms by replacing regularization

proximals (traditionally based on sparsity/low-rank) with expressive, data-driven DAE updates. PnP methods decouple the physical acquisition model from learned image priors, enabling scan-specific (zero-shot) reconstruction without retraining for different acquisition settings. Unlike prior PnP approaches trained on limited qMRI/MRF data [12], [28], we use DAEs pretrained on routine weighted-MRI datasets, and incorporate them into MRF reconstruction via MRI synthesis.

III. MRI2QMAP

We propose an augmented Lagrangian formulation for qMRI/MRF reconstruction integrated with MRI-driven priors:

$$\begin{aligned} \mathcal{L}_k(\mathbf{x}, \mathbf{q}, \mathbf{m}, \mathbf{u}, \mathbf{w}) := & f(\mathbf{x}) + \frac{\mu_k}{2} \|\mathbf{x} - \mathcal{B}^{\mathcal{Q}}(\mathbf{q}) + \mathbf{u}\|_2^2 \\ & + \sum_{i \in \mathcal{M}} \frac{\mu_k \gamma_i}{2} \|\mathbf{m}_i - \mathcal{B}^{\mathcal{W}}(\mathbf{q})_i + \mathbf{w}_i\|_2^2 + \alpha_i \mathcal{R}_i(\mathbf{m}_i) \end{aligned} \quad (7)$$

The goal is to reconstruct multi-parametric qmaps \mathbf{q} , the TSMI \mathbf{x} , and spatially-restored synthesized MRI images $\mathbf{m} = \{\mathbf{m}_i\}_{i \in \mathcal{M}}$ in contrast modalities $\mathcal{M} = \{\text{T1w}, \text{T2w}, \text{PDw}\}$. \mathbf{u}, \mathbf{w} are scaled Lagrange multipliers that are iteratively updated along with alternating minimization of \mathcal{L}_k over $\mathbf{x}, \mathbf{q}, \mathbf{m}$ using ADMM algorithm iterations k [39]. The first term $f(\mathbf{x}) := \frac{1}{2} \|\mathbf{y} - \mathcal{A}\mathbf{x}\|_2^2$ enforces k-space consistent TSMI, the second term enforces TSMI-consistent qmaps via MRF Bloch response model (2), and the third term enforces MRI-consistent qmaps via synthesis model (4). The regularizers \mathcal{R}_i impose modality-specific spatial priors on the synthesized MRI images, thereby restoring them and the linked qmaps under undersampling artifacts. Hyperparameters $\mu_k, \gamma_i, \alpha_i := \lambda \gamma_i, \lambda > 0$ balance between terms and regularization.

A. The algorithm

MRI2Qmap (Algorithm 1) adopts a plug-and-play ADMM framework [40] with three key steps at each iteration:

1) *Updating k-space consistent TSMI*: minimizes (7) over \mathbf{x} while other variables fixed at their current estimates (Line 10):

$$\begin{aligned} \mathbf{x}^k \leftarrow & \text{prox}_f(\mathcal{B}^{\mathcal{Q}}(\mathbf{q}) - \mathbf{u}, \mu_k^{-1}) \\ = & (\mathcal{A}^H \mathcal{A} + \mu_k \mathbf{I})^{-1} (\mathcal{A}^H \mathbf{y} + \mu_k (\mathcal{B}^{\mathcal{Q}}(\mathbf{q}) - \mathbf{u})). \end{aligned} \quad (8)$$

Here, $\text{prox}_h(\tilde{\mathbf{x}}, \tau) := \arg\min_{\mathbf{x}} \frac{1}{2} \|\mathbf{x} - \tilde{\mathbf{x}}\|_2^2 + \tau h(\mathbf{x})$ denotes the proximal operator of a function h with shrinkage parameter $\tau > 0$. For the least-squares data-fidelity term f , prox_f reduces to solving a linear system, which can be updated using a few conjugate-gradient (CG) iterations [36].

2) *MRI synthesis and restoration*: At each iteration, multi-modal weighted-MRI images are synthesized from the current qmaps via $\mathcal{B}^{\mathcal{W}}(\mathbf{q})$ and restored spatially (Line 8) using a conditional MRI denoiser (DAE_{MRI}) capable of operating across multiple specified MRI contrasts and Gaussian noise levels. The denoiser is trained on unpaired MRI datasets from diverse subjects, covering the contrast modalities \mathcal{M} , and spatial resolutions and anatomies relevant to the MRF imaging task (see Section III-B). Following [37], we employ an annealed denoising schedule with parameters σ_k , logarithmically spaced across iterations from $\sigma_1 = \sigma_{\max}$ to $\sigma_K = \sigma_{\min}$, which

enables faster reconstructions (Section IV-C4). The denoiser serves as a plug-and-play replacement for the proximal operator of the regularizer in the \mathbf{m} -minimizing step of (7) i.e., $\text{prox}_{\mathcal{R}_i}(\mathcal{B}^{\mathcal{W}}(\mathbf{q})_i - \mathbf{w}_i, \sigma_k^2)$ with $\sigma_k = \sqrt{\lambda/\mu_k}$, imposing data-driven spatial priors on synthesized MRI modalities.

3) *Combined MRF-MRI dictionary matching*: The \mathbf{q} -minimizing step updates the quantitative maps by enforcing joint consistency with the TSMI and the spatially-restored synthesized MRI images:

$$\arg\min_{\mathbf{q}} \|\mathbf{x} + \mathbf{u} - \mathcal{B}^{\mathcal{Q}}(\mathbf{q})\|_2^2 + \|\mathbf{m} + \mathbf{w} - \mathcal{B}^{\mathcal{W}}(\mathbf{q})\|_{\gamma}^2. \quad (9)$$

Here, $\|x\|_{\gamma}^2 := \text{trace}(x^H \text{diag}(\gamma)x)$ denotes a row-wise weighted squared norm for a matrix, where the weights $\gamma := \{\gamma_i\}_{i \in \mathcal{M}}$ control the relative contributions of different MRI contrasts with respect to the TSMI in quantitative mapping. The objective is voxel-wise separable, which allows to extend dictionary matching to approximate this step. Specifically, two dictionaries are precomputed from the Bloch models (2) and (4): the MRF dictionary $D^{\mathcal{Q}} \in \mathbb{C}^{s \times d}$ and the multimodal MRI dictionary $D^{\mathcal{W}} \in \mathbb{R}^{s' \times d}$, both generated over a shared LUT of d sampled T1-T2 pairs, where $\forall j \in \text{LUT}, D_j^{\mathcal{Q}} := \text{BLOCH}^{\mathcal{Q}}(j)$ and $D_j^{\mathcal{W}} := \text{BLOCH}^{\mathcal{W}}(j)$. Given a TSMI-MRI image pairs $(\tilde{\mathbf{x}}, \tilde{\mathbf{m}}) \in \mathbb{C}^{s \times n} \times \mathbb{R}^{s' \times n}$, the combined *MRF-MRI dictionary matching* (Line 9) is defined for each voxel v as:

$$\begin{aligned} \mathbf{q}_v^* = & \text{D-MATCH}((\tilde{\mathbf{x}}_v, \tilde{\mathbf{m}}_v), (D^{\mathcal{Q}}, D^{\mathcal{W}}), \gamma) \\ := & \arg\min_{j \in \text{LUT}, \text{PD} \in \mathbb{C}} \|\tilde{\mathbf{x}}_v - \text{PD} \cdot D_j^{\mathcal{Q}}\|_2^2 + \|\tilde{\mathbf{m}}_v - |\text{PD}| \cdot D_j^{\mathcal{W}}\|_{\gamma}^2 \end{aligned}$$

with closed-form solutions (proof in Section S.I):

$$(\text{T1}_v^*, \text{T2}_v^*) = j_v^* = \arg\max_{j \in \text{LUT}} \frac{|\langle D_j^{\mathcal{Q}}, \tilde{\mathbf{x}}_v \rangle| + \langle D_j^{\mathcal{W}}, \tilde{\mathbf{m}}_v \rangle_{\gamma}}{\sqrt{\|(D_j^{\mathcal{Q}}\|_2^2 + \|D_j^{\mathcal{W}}\|_{\gamma}^2)}, \quad (10)$$

$$\text{PD}_v^* = \frac{\langle D_{j_v^*}^{\mathcal{Q}}, \tilde{\mathbf{x}}_v \rangle}{|\langle D_{j_v^*}^{\mathcal{Q}}, \tilde{\mathbf{x}}_v \rangle|} \cdot \frac{|\langle D_{j_v^*}^{\mathcal{Q}}, \tilde{\mathbf{x}}_v \rangle| + \langle D_{j_v^*}^{\mathcal{W}}, \tilde{\mathbf{m}}_v \rangle_{\gamma}}{\|(D_{j_v^*}^{\mathcal{Q}}\|_2^2 + \|D_{j_v^*}^{\mathcal{W}}\|_{\gamma}^2)}. \quad (11)$$

Here, $\langle x, \tilde{x} \rangle_{\gamma} := \text{trace}(x^H \text{diag}(\gamma)\tilde{x})$ denotes a weighted inner product. Setting $\gamma = \mathbf{0}$ recovers standard MRF-only dictionary matching as in (3) and [16], and disables the coupling between qmaps and MRI-domain priors. Following qmap estimation, updated TSMI and MRI images, $\mathcal{B}^{\mathcal{Q}}(\mathbf{q})$ and $\mathcal{B}^{\mathcal{W}}(\mathbf{q})$, are generated using their respective dictionary approximations.

Lines 11–12 update the ADMM Lagrange multipliers \mathbf{u}, \mathbf{w} , while Lines 7/13 obtain their scaled/unscaled forms according to the penalty parameters μ_k , following [39, Chapter 3]. For initialization (Lines 1–5), we perform a few CG iterations to minimize the k-space loss $f(\mathbf{x})$ to obtain \mathbf{x}_{init} , followed by standard MRF dictionary matching to obtain \mathbf{q}_{init} . Following [37], Line 5 defines an increasing sequence for μ_k across iterations, determined by the user-specified annealed denoising schedule σ_k and regularization parameter λ . Finally, because the MRF and MRI Bloch responses may differ in scale across modalities, we normalize the modality-wise weights γ by the relative norms of the TSMI and the synthesized MRI contrasts (Line 4) and use the normalized weights $\bar{\gamma}_{i \in \mathcal{M}} \in [0, 1]$ as algorithm input to control the MRF–MRI dictionary matching.

B. Implementation details

1) *Training the MRI denoiser*: Our approach was developed in PyTorch.¹ The MRI denoiser DAE_{MRI} is a modality-conditional 3D residual UNet derived from the guided-diffusion toolbox [41]. The model operates on 3D patches (size 64^3) and conditions on MRI contrast (T1w, T2w, PDw) via class embeddings. The model is also conditioned on discretized noise levels through a noise-level embedding; specifically, 25 Gaussian noise levels Σ logarithmically spaced within $[0.02, 0.5]$ were used during training, spanning negligible noise to the upper effective range observed in our reconstruction experiments. The UNet employs five resolution levels with two residual blocks per level, channel widths $[64, 128, 256, 512, 512]$ from highest to lowest spatial resolutions, and attention layers (4 heads) at 16^3 and 8^3 feature resolutions. Training/inference was performed in fp16 mixed precision for improved computational efficiency.

The denoiser was trained on an unpaired MRI dataset comprising 3000 3D brain volumes assembled from 1000 T1w and 1000 T2w scans from the Human Connectome Project (1200 Subjects Release) [42], and 500 PDw scans (sampled twice to balance modalities) from the IXI dataset [43]. All volumes were resampled to 1 mm^3 isotropic resolution, aligned to the MRF acquisition orientation, and intensity-normalized by scaling the 99.5th percentile to unity. Data augmentation (via MONAI [44]) included smoothly varying bias-field distortions, random intensity scaling up to $\pm 50\%$, and random cropping into 64^3 patches at each iteration. Gaussian noise with standard deviation $\sigma \sim \mathcal{U}(\Sigma)$ randomly drawn from discretized noise levels, was added to each training patch. Residual learning was adopted via the parameterization $\text{DAE}_{\text{MRI}}(\tilde{m}, i, \sigma^2) := \tilde{m} - \epsilon_\theta(\tilde{m}, i, \sigma^2)$ where the network ϵ_θ predicts the injected noise, given the noisy image \tilde{m} , modality label $i \in \mathcal{M}$, and noise level σ . The network was trained to minimize an MSE loss between the true and predicted noise, using ADAM optimizer (learning rate 10^{-4} , batch size 4) for 1000 epochs.

2) *Reconstruction parameters*: Experiments were conducted on a multicoil *in-vivo* dataset and a single-coil simulated brain dataset using non-Cartesian MRF acquisitions from [5].

To accelerate the CG updates (Line 10), the $\mathcal{A}^H \mathcal{A}$ operations employed a Toeplitz approximation [45] with spatiotemporal kernels [5], [46]. Similar to [36] we found that the CG subproblems do not require high-precision convergence (Section S.IV-C). The number of ADMM iterations K and inner CG iterations K_{cg} depending on the conditioning of $\mathcal{A}^H \mathcal{A}$, were set to $K = K_{cg} = 10$ in multicoil and $K = 60, K_{cg} = 20$ in single-coil experiments. For MRI synthesis $\mathcal{B}^{\mathcal{W}}(\mathbf{q})$, we used the spin-echo signal model in (5) with experimentally selected TR/TE settings of $(500\text{ms}, 0)$, $(\infty, 100\text{ms})$ and $(\infty, 0)$ for T1w, T2w, and PDw contrasts, respectively. Additional TR/TE configurations were evaluated in Section IV-C2, with reconstruction performance remaining stable across relevant parameter ranges. The regularization parameter λ was set to 2×10^{-6} for *in-vivo* experiments and 10^{-6} for simulated data. Equal modality weights ($\bar{\gamma}_i = 0.3, \forall i \in \mathcal{M}$) were used for

Algorithm 1 MRI2Qmap

Input: $\mathbf{y}, \mathcal{A}, \text{DAE}_{\text{MRI}}, D^{\mathcal{Q}}, D^{\mathcal{W}}$ (from $\mathcal{B}^{\mathcal{Q}}, \mathcal{B}^{\mathcal{W}}$)
params: $\{\sigma_k\}_{k=1}^K, \{\bar{\gamma}_i\}_{i \in \mathcal{M}}, \lambda > 0$, MRI modalities \mathcal{M}

- 1: $\mathbf{u} = \mathbf{w} = \mathbf{0}$
- 2: $\mathbf{x} = \mathbf{x}_{\text{init}} = (\mathcal{A}^H \mathcal{A})^{-1} \mathcal{A}^H \mathbf{y}$
- 3: $\mathbf{q} = \mathbf{q}_{\text{init}} = \text{D-MATCH}(\mathbf{x}, D^{\mathcal{Q}})$
- 4: $\gamma := \left\{ \bar{\gamma}_i \frac{\|\mathcal{B}^{\mathcal{Q}}(\mathbf{q})\|_2^2}{\|\mathcal{B}^{\mathcal{W}}(\mathbf{q})\|_2^2} \right\}_{i \in \mathcal{M}}$
- 5: $\forall k: \mu_k := \lambda / \sigma_k^2$
- 6: **for** $k = 1 : K$
- 7: $\mathbf{u} \leftarrow \mu_k^{-1} \mathbf{u}, \mathbf{w} \leftarrow \mu_k^{-1} \mathbf{w}$
- 8: $\forall i \in \mathcal{M}: \mathbf{m}_i \leftarrow \text{DAE}_{\text{MRI}}(\mathcal{B}^{\mathcal{W}}(\mathbf{q})_i - \mathbf{w}_i, i, \sigma_k^2)$
- 9: $\mathbf{q} \leftarrow \text{D-MATCH}((\mathbf{x} + \mathbf{u}, \mathbf{m} + \mathbf{w}), (D^{\mathcal{Q}}, D^{\mathcal{W}}), \gamma)$
- 10: $\mathbf{x} \leftarrow (\mathcal{A}^H \mathcal{A} + \mu_k \mathbf{I})^{-1} (\mathcal{A}^H \mathbf{y} + \mu_k (\mathcal{B}^{\mathcal{Q}}(\mathbf{q}) - \mathbf{u}))$
- 11: $\mathbf{u} \leftarrow \mathbf{u} + \mathbf{x} - \mathcal{B}^{\mathcal{Q}}(\mathbf{q})$
- 12: $\mathbf{w} \leftarrow \mathbf{w} + \mathbf{m} - \mathcal{B}^{\mathcal{W}}(\mathbf{q})$
- 13: $\mathbf{u} \leftarrow \mu_k \mathbf{u}, \mathbf{w} \leftarrow \mu_k \mathbf{w}$
- 14: **end for**

return \mathbf{q} (qmaps), \mathbf{x} (TSMI), \mathbf{m} (synthesized MRIs).

dictionary matching. The base model employed exact dictionary search, with ablation results (Section IV-C6) showing that approximate search can further optimize runtime.

Annealed denoising schedules, logarithmically spaced between $\sigma_1 = 0.2$ and $\sigma_K = 0.02$ and rounded to the nearest levels in Σ , were used and provided best reconstruction runtime-accuracies (Section IV-C4). At each MRI2Qmap iteration, the three-modality MRI inputs to DAE_{MRI} were intensity-normalized, then shifted with random spatial offsets from $\mathcal{U}([-32, 32]^3)$ as a reconstruction-time augmentation. The shifted volumes were partitioned into non-overlapping 64^3 patches, denoised, and reassembled, followed by inverse shifting and intensity rescaling to produce Line 8 outputs. Except denoising, other steps were performed in single precision.

IV. NUMERICAL EXPERIMENTS

To evaluate the effectiveness of our method, we benchmark MRI2Qmap against representative MRF reconstruction baselines on two datasets: *in-vivo* and simulated 3D brain acquisitions, both based on the TGAS-SPI-MRF protocol [5] with 8-fold k-space undersampling. All methods were implemented in PyTorch and run on a workstation with an Intel Core i9 CPU and a single NVIDIA RTX A6000 GPU.

A. Experimental setup

1) *In-vivo data*: We used 3D MRF brain data from [11], acquired with the TGAS-SPI-MRF sequence on a 3T Premier scanner (GE Healthcare) using a 48-channel receive coil, at 1 mm^3 isotropic resolution and reconstructed to 256^3 voxels. The gold-standard acquisition ($R = 1$) used 48 readout groups (each sampling different k-space locations) to achieve dense k-space coverage within a 6-min scan. Each group consisted of an inversion pulse followed by a variable flip-angle schedule ($10\text{--}75^\circ$; TI/TE/TR = 20/0.7/12 ms) over $l = 500$ timeframes with non-Cartesian 3D spiral k-space sampling trajectories. Following a similar scheme as [5], six readout groups ($R = 8$)

¹Source codes will be released upon acceptance.

Data/Method	MAPE (%) ↓			CD × 10 ⁻³ ↓	PSNR (dB) ↑			SSIM (%) ↑			
	T1+T2	T1	T2		TSMI	T1w	T2w	PDw	T1w	T2w	PDw
<i>In-vivo</i>	SVDMRF	44.40	14.97 (0.94)	29.44 (2.22)	–	–	–	–	–	–	–
	ADMM	23.14	9.40 (0.79)	13.73 (1.27)	2.92 (0.50)	32.18 (0.62)	27.23 (0.65)	27.81 (0.60)	94.45 (0.78)	91.35 (1.05)	86.85 (1.20)
	LLR	16.17	8.38 (0.59)	7.79 (0.66)	3.25 (0.41)	32.93 (0.51)	28.44 (0.59)	29.09 (0.49)	95.13 (0.68)	92.97 (0.98)	86.43 (1.09)
	LRTV	14.18	6.53 (0.43)	7.65 (0.58)	2.71 (0.38)	33.53 (0.46)	28.84 (0.55)	30.58 (0.45)	97.02 (0.42)	93.98 (0.72)	90.65 (0.76)
	MRI2Qmap	12.01	4.93 (0.34)	7.08 (0.50)	0.85 (0.11)	35.91 (0.45)	30.03 (0.49)	30.63 (0.52)	97.95 (0.30)	95.26 (0.58)	91.42 (0.94)
	ARNet*	12.82	5.61 (0.44)	7.21 (0.63)	1.14 (0.20)	35.83 (0.69)	30.33 (0.76)	31.74 (0.87)	97.79 (0.33)	95.31 (0.65)	92.99 (0.92)
MRF-PnP*	12.81	5.39 (0.51)	7.42 (0.71)	1.57 (0.33)	36.33 (0.80)	30.53 (0.81)	32.37 (0.74)	97.76 (0.43)	95.37 (0.78)	93.25 (0.81)	
<i>BrainWeb</i>	SVDMRF	254.95	70.79 (8.12)	184.16 (25.66)	–	–	–	–	–	–	–
	ADMM	36.08	12.74 (1.12)	23.34 (2.24)	5.94 (1.02)	26.47 (0.69)	24.85 (0.61)	26.29 (0.72)	89.77 (0.75)	88.60 (1.13)	79.14 (0.99)
	LLR	22.57	8.21 (0.48)	14.36 (0.98)	3.31 (0.47)	27.52 (0.46)	27.20 (0.27)	27.80 (0.62)	90.39 (0.47)	92.59 (0.50)	81.69 (0.86)
	LRTV	19.22	7.32 (0.57)	11.89 (1.08)	2.78 (0.46)	29.16 (0.55)	27.12 (0.58)	29.16 (0.80)	95.88 (0.50)	93.93 (0.96)	86.49 (1.15)
	MRI2Qmap	8.97	3.27 (0.15)	5.70 (0.42)	0.61 (0.06)	32.33 (0.54)	32.51 (0.27)	32.98 (0.51)	98.82 (0.10)	97.96 (0.15)	95.90 (0.53)
	ARNet*	9.92	3.05 (0.14)	6.87 (0.73)	1.02 (0.10)	31.90 (1.06)	27.37 (1.42)	31.49 (1.34)	97.99 (0.20)	94.59 (2.13)	94.53 (0.80)
MRF-PnP*	8.25	3.01 (0.09)	5.24 (0.54)	0.56 (0.05)	34.59 (0.88)	33.84 (0.42)	34.48 (0.76)	99.00 (0.08)	98.46 (0.16)	97.68 (0.23)	

TABLE I: Mean (\pm SD) performance on *in-vivo* and BrainWeb datasets at $R = 8$. (*) indicates methods trained with ground-truth MRF maps. MRI2Qmap performs competitively with MRF-supervised baselines and outperforms remaining methods.

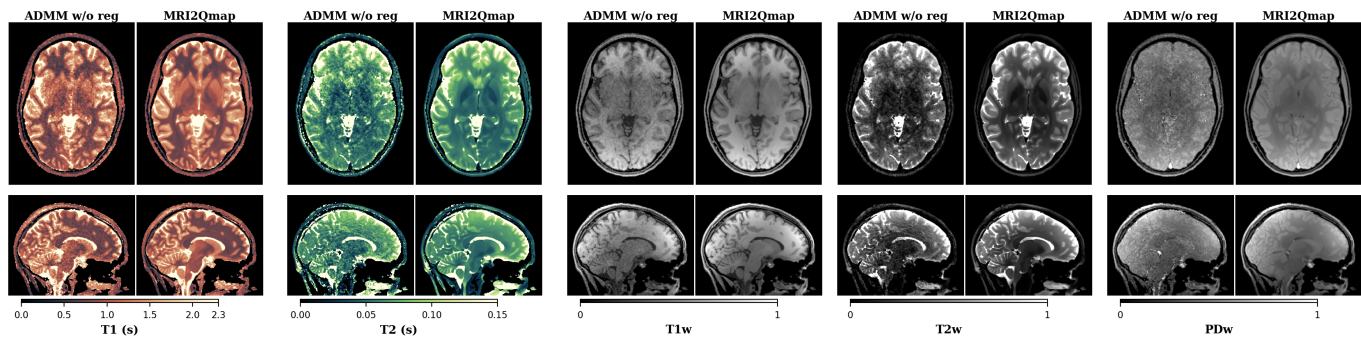


Fig. 1: MRI2Qmap vs. an ADMM reconstruction without spatial regularization. Quantitative T1/T2 maps and synthesized T1w, T2w, and PDw images are shown (electronic zoom recommended). By leveraging MRI-driven denoising priors, MRI2Qmap suppresses aliasing artifacts in synthesized contrasts and the underlying quantitative maps.

were retrospectively subsampled to create highly accelerated sub-minute acquisitions. Data from 11 subjects were evaluated. Reconstructions from the densely sampled 6-min scans ($R = 1$) served as reference, obtained via [6] enforcing joint k-space and Bloch consistency. While our method does not require MRF training data, the tested deep learning baselines (ARNet, MRF-PnP) do. For these methods, we used a leave-one-subject-out strategy: for each test subject, the remaining 10 subjects were used for training, resulting in 11 separately trained models and a corresponding 11-fold evaluation.

Pre-processing followed the toolbox in [11], including density compensation, field-of-view adjustment, compression to $c = 10$ virtual coils, and sensitivity map estimation. The MRF dictionary ($\sim 26k$ atoms, $(T_1, T_2) \in [20, 5000] \times [10, 4000]$ ms) with SVD-based temporal compression from $l = 500$ frames to $s = 5$ coefficient channels [15] was also adopted.

2) *Simulated brain data*: Simulated data was generated from 3D qmaps (T1, T2, PD; 1 mm^3 resolution, 256^3 voxels), using MRtwin [47] and multi-subject anatomical brain models from BrainWeb database [48] (see Appendix S.II). These qmaps served as ground truth and were used to create MRF time-series data from the same TGAS-SPI-MRF sequence and Bloch dictionary. Gaussian noise at 25% of the mean signal amplitude was added to each TSMI. Single-coil MRF measurements were simulated using the same $R = 8$ k-space

trajectories as in the *in-vivo* study. Data from 10 subjects were used for evaluation; an additional 10 BrainWeb subjects were used to train deep-learning baselines (ARNet, MRF-PnP).

3) *Baselines*: MRI2Qmap with settings described in section III-B was compared to the following baselines: **SVDMRF** [15] uses gridding/adjoint operator $\mathbf{x}_{\text{grid}} = \mathcal{A}^H \mathbf{y}$ to estimate the TSMI. **MRF-ADMM** [6] uses ADMM for TSMI reconstruction by enforcing k-space fidelity and Bloch/dictionary constraints i.e., the first two terms of (7), without spatial regularization. For comparisons, reconstruction parameters $(\mathbf{x}_{\text{init}}, K, K_{cg}, \mu)$ were matched to those of MRI2Qmap. **LLR** [5] and **LRTV** [8] are convex baselines solving $\min_{\mathbf{x}} f(\mathbf{x}) + \mathcal{R}(\mathbf{x})$ with k-space fidelity and locally low-rank or total variation TSMI priors, respectively. Both methods use FISTA [49]; LRTV applies the Chambolle-Pock proximal, while LLR uses singular-value soft-thresholding, with all proximal steps GPU accelerated. **Artifact Removal Network (ARNet)** is a supervised deep learning baseline trained to remove undersampling artifacts from initial TSMI reconstructions from $R = 8$ acquisitions. Training used paired MRF data: inputs were randomly cropped 64^3 patches from CG-reconstructed $R = 8$ TSMI (\mathbf{x}_{init} in Algorithm 1, Line 2), and targets were the corresponding reference TSMIs derived from ground-truth qmaps (BrainWeb) or from long, densely sampled $R = 1$ MRF acquisitions (*in-vivo*). Several archi-

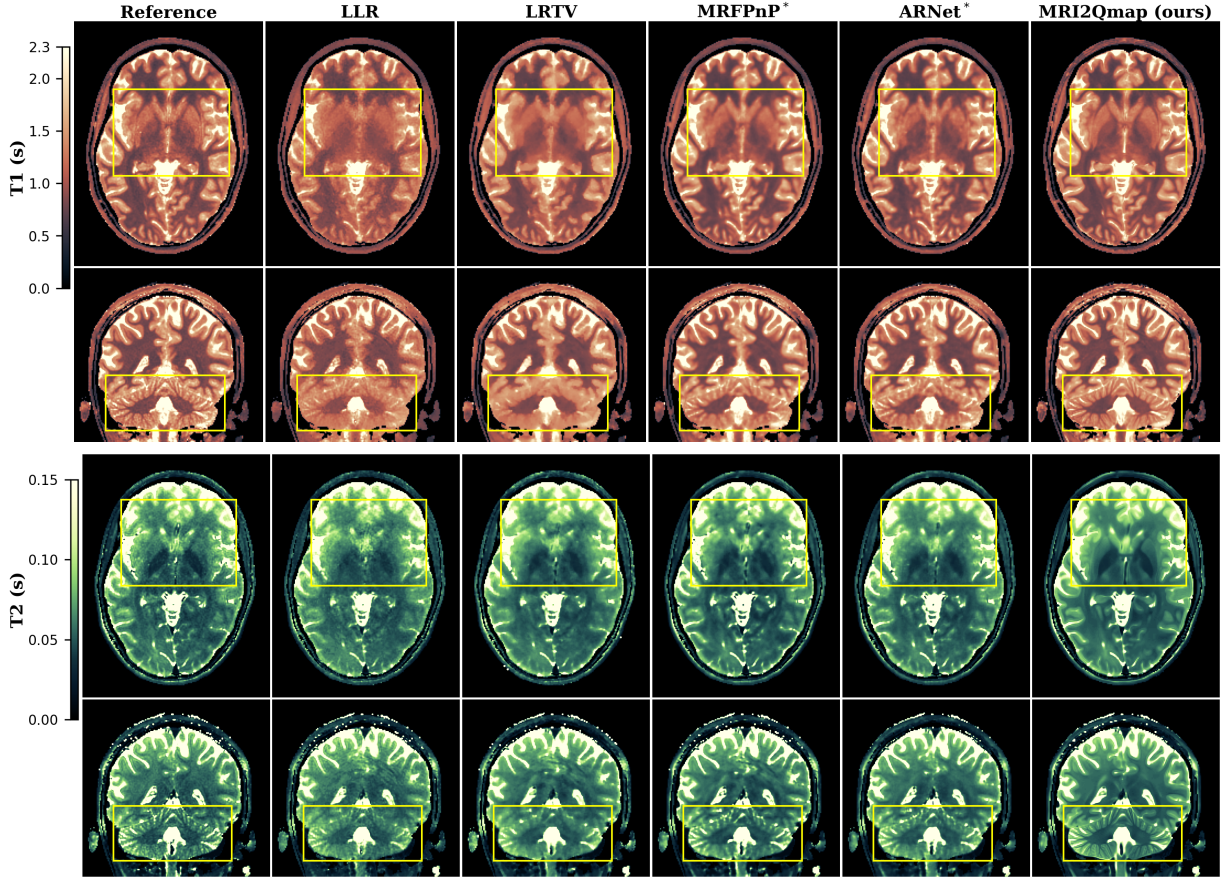


Fig. 2: Reconstructed T1 and T2 maps at $R = 8$ acceleration. Relative to baselines (*indicates MRF-trained), MRI2Qmap exhibits reduced artifacts and improved anatomical delineation e.g. for deep brain structures (axial views) and the cerebellum (coronal views). Electronic zoom in boxed regions is recommended.

textures have been proposed for this or closely-related tasks (see section I-A2); For comparability, ARNet used the same UNet backbone as MRI2Qmap, with modified input/output channels. **PnP-MRF** [28] is a plug-and-play ADMM method for TSMI reconstruction that combines k-space data fidelity with a TSMI denoising prior. Unlike MRI2Qmap, the denoiser operates directly on MRF timeframe data and was trained to remove simulated Gaussian noise from 64^3 patches of reference TSMIs obtained via ground-truth qmaps (BrainWeb) or $R = 1$ acquisitions (*in-vivo*). Reconstructions from $R = 8$ data alternated CG-based kspace fidelity with TSMI denoising, using same initialization and iterations count as MRI2Qmap.

For each ARNet/PnP-MRF baseline, twelve models were trained and evaluated: one for BrainWeb data, and eleven for *in-vivo* subjects using leave-one-subject-out validation. Quantitative maps were obtained via standard MRF dictionary matching post hoc to all reconstructed TSMIs. All baselines used GPU acceleration and Toeplitz forward–adjoint approximations; see Supplementary Section S.III for details.

4) *Evaluation Metrics*: T1 and T2 mapping performances were assessed using mean absolute percentage error (MAPE) over diagnostically relevant white- and gray-matter regions: $\text{MAPE} := \mathbb{E}_{v \in M} \frac{|\hat{q}_v - q_v|}{|q_v|}$, where \hat{q}, q denote estimated and reference maps, v indexes voxels, and M is the anatomical mask. For BrainWeb experiments, masks were obtained di-

rectly from [48], whereas for *in-vivo* data they were derived by segmenting reference images using [50]. TSMI reconstruction quality was measured using cosine distance, $\text{CD} := 1 - \frac{|\langle \hat{\mathbf{x}}_v, \mathbf{x}_v \rangle|}{\|\hat{\mathbf{x}}_v\|_2 \|\mathbf{x}_v\|_2}$. Synthesized MRI images from predicted and reference qmaps were compared using PSNR and SSIM, averaged over 50 central axial slices, with air/background suppressed by thresholding low proton-density regions.

B. Results

Tables I compares MRI2Qmap with baseline methods on *in-vivo* and BrainWeb datasets. SVD-MRF shows the largest errors due to gridding-based inversion approximation (for this method, only T1/T2 mapping metrics are reported). MRF-ADMM improves upon this via iterative optimization; however, under highly undersampled acquisitions and without spatial regularization, its performance remains limited. LLR and LRTV further enhance reconstruction quality by incorporating spatial-domain priors; however, both are consistently outperformed by MRI2Qmap, which exploits learned MRI-domain priors. On the other hand, MRI2Qmap achieves results that are competitive with supervised MRF-domain baselines (ARNet and PnP-MRF), despite not being trained on ground-truth MRF data. Differences between MRI2Qmap and these baselines are generally small, with MRI2Qmap showing sim-

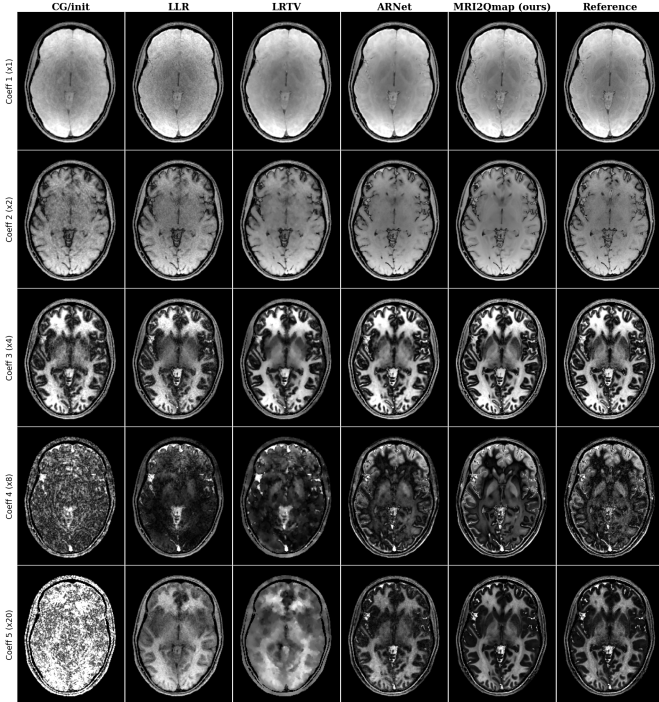


Fig. 3: TSMI magnitudes across $s = 5$ compressed coefficient channels (rows) for the subject in Fig.2, reconstructed by MRI2Qmap and baselines (columns). CG/init \mathbf{x}_{init} initializes MRI2Qmap; ARNet was trained with MRF ground-truth data.

ilar or in certain metrics marginally improved performance, e.g., for T1/T2 and TSMI estimation for *in-vivo* data.

Qualitative comparisons are further shown in Figs. 1, 2, 3 for an *in-vivo* test subject. Fig.1 compares MRI2Qmap and MRF-ADMM across reconstructed T1/T2 maps and the corresponding synthesized weighted MRI volumes; The two methods differ only in the inclusion of MRI priors in MRI2Qmap. While MRF-ADMM shows pronounced aliasing artifacts, MRI2Qmap effectively mitigates them, producing cleaned synthesized weighted images and, thanks to exploiting cross-domain MRF–MRI relationships, restored underlying T1/T2 maps. Figure 2 extends the comparison to additional baselines (SVDMMRF excluded due to poor performance). MRI2Qmap better preserves anatomical details and tissue boundaries, as seen in highlighted regions, including deep brain structures (e.g. putamen, pallidum, caudate) in axial views and the cerebellum in coronal views, for both T1/T2 maps. LLR/LRTV show noticeable over-smoothing, with residual aliasing particularly in T2 maps. Supervised MRF-domain baselines (e.g. ARNet) improve upon LLR/LRTV but tend to produce noisier maps with less well-defined tissue boundaries compared to MRI2Qmap, which may partly reflect the limited quality of their training targets from 6-min MRF acquisitions that are still somewhat undersampled and noisier than standard MRI data used for training MRI2Qmap. A similar trend is observed in the TSMI reconstructions (Fig.3), where the last three channels, the weakest and most challenging to recover, are better reconstructed by MRI2Qmap than the baselines, with clear improvement over the initialization \mathbf{x}_{init} , highlighting the effectiveness of MRI-domain priors. Overall, these

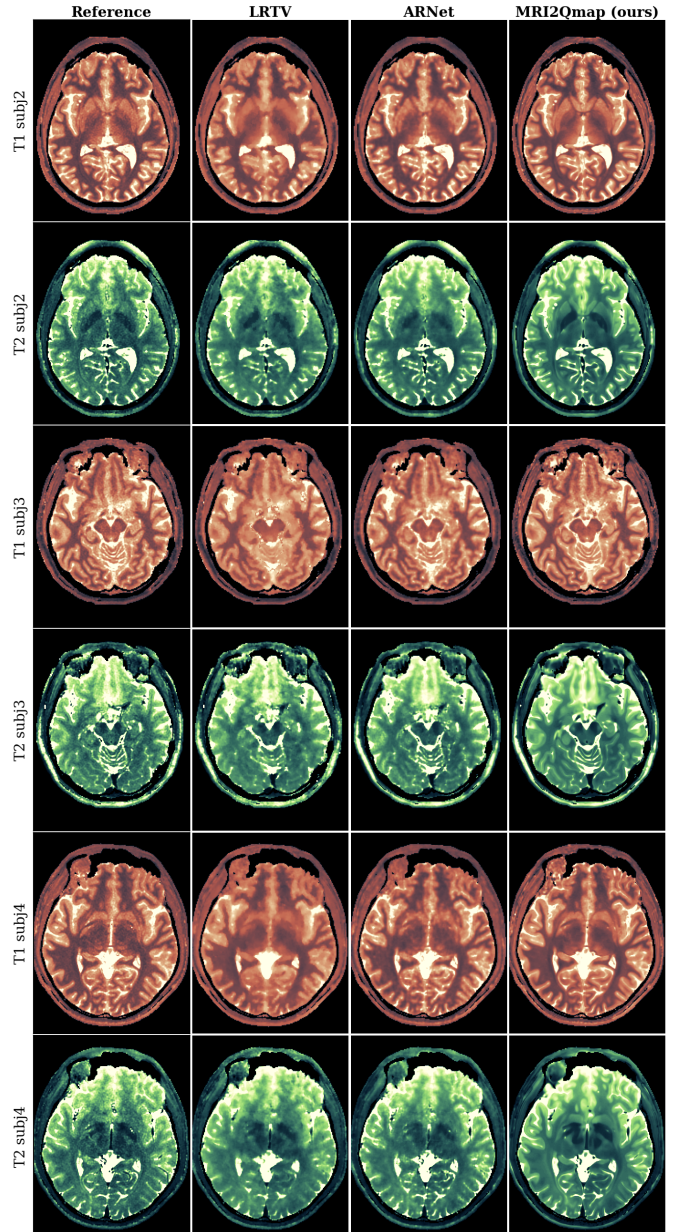


Fig. 4: Reconstructed T1/T2 maps for additional *in-vivo* subjects: MRI2Qmap vs. representative baselines (LRTV/ARNet).

results demonstrate that MRI2Qmap achieves high-quality quantitative reconstructions without relying on ground-truth MRF training data. Additional reconstructions from other test subjects are shown in Fig. 4, with further *in-vivo* and BrainWeb examples provided in Figs S.1, S.2 and S.3.

C. Discussion

Here we study the impact of key MRI2Qmap design choices via ablation experiments, focusing on MRI denoising modalities, synthesis parameters, and runtime-related factors, followed by a discussion of limitations and future work.

1) *MRI denoising modalities*: We assess the contribution of each MRI modality prior used in MRI2Qmap by disabling individual contrasts (T1w, T2w, PDw) via setting their weights small $\bar{\gamma}_i = 10^{-10}$, while other parameters unchanged. Table II

MRI2Qmap Modalities	MAPE (%) ↓			PSNR (dB) ↑		
	T1+T2	T1	T2	T1w	T2w	PDw
All (base)	12.01	4.93	7.08	35.91	30.03	30.63
T2w PDw	14.59	7.50	7.09	33.75	29.94	30.66
T1w PDw	16.51	4.77	11.74	36.05	27.96	31.07
T1w T2w	19.19	10.44	8.75	36.01	29.36	27.28

TABLE II: MRI2Qmap performance with all or partial MRI modality priors, averaged over *in-vivo* data.

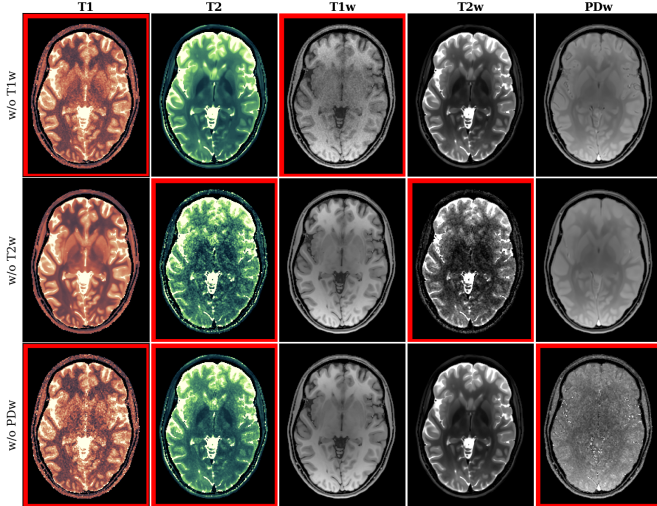


Fig. 5: T1/T2 maps and synthesized MRIs (columns) from MRI2Qmap with one denoising modality prior disabled (rows); most affected images in each row are highlighted.

reports average T1/T2 mapping MAPEs and synthesized MRI PSNRs on the *in-vivo* dataset, compared with the base model using all contrasts (Fig 5 shows qualitative results). Using denoising priors from all three modalities gives the lowest combined T1+T2 error. Excluding T1w priors primarily degrades T1 and T1w accuracies, while excluding T2w priors mostly impacts T2 and T2w reconstructions. Removing the PDw prior increases both T1 and T2 errors, which is expected since MR signal evolutions depend jointly on proton density, and inaccurate PD estimation propagates to errors in T1 and T2 even when T1w and T2w priors are present.

2) *MR synthesis parameters*: We examined the sensitivity of MRI2Qmap to the spin-echo synthesis parameters TR (T1w) and TE (T2w). The base model used TR = 500 ms for T1w and TE = 100 ms for T2w synthesis, chosen within typical clinical ranges (TR: 300–800 ms; TE: 80–120 ms). Robustness of T1/T2 mapping was evaluated on *in-vivo* dataset by independently varying TR and TE from $0.5\times$ to $2\times$ their base values, with keeping other parameters fixed. As shown in Fig. 6, reconstruction accuracy is slightly more sensitive to TE (T2w) than TR (T1w), yet remains overall stable, with combined T1+T2 MAPE varying by less than 0.2% within clinically relevant ranges (dashed lines).

3) *Runtime/memory comparison*: Table III reports reconstruction times and GPU memory usage of MRI2Qmap (base model) and selected baselines on *in-vivo* data, and further decomposes the per-iteration cost of MRI2Qmap across its main components. The CG-based $prox_f$ step dominates both runtime and memory, followed by MRI denoising and dic-

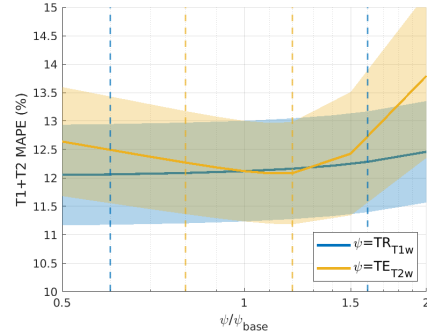


Fig. 6: MRI2Qmap mapping performance on *in-vivo* data vs. T1w TR (blue) and T2w TE (orange) variations relative to the default synthesis values ($TR_{base}/TE_{base} = 500/100$ ms). Solid lines and shaded regions show mean MAPE \pm standard deviation. Dashed lines mark practical parameter ranges.

	Total cost					MRI2Qmap cost/iter.		
	LLR	LRTV	MRFPnP	ARNet	MRI2Qmap	Prox	DM	DN
Runtime \approx	778	528	547	89	684	40.1	9.9	10.6
GPU Mem.	33.9	33.9	36.9	34.8	36.9	36.9	19.5	26.5

TABLE III: (Left) Reconstruction times (s) and peak GPU memory (GB) usage of each method, averaged over *in-vivo* data. (Right) MRI2Qmap average per-iteration cost breakdown for $prox_f$, dictionary matching (DM), and denoising (DN).

tionary matching. ARNet achieves the fastest reconstruction, as it is non-iterative beyond CG initialization and does not enforce k-space consistency. Other methods using iterative forward–adjoint operations to minimize k-space loss incur longer but overall comparable runtimes, with MRI2Qmap taking ~ 11 minutes on a single GPU to reconstruct a 3D brain volume at 1 mm^3 resolution from multicoil non-Cartesian data. Studies below further analyze runtime factors in MRI2Qmap.

4) *Annealed denoising schedule*: We compare fixed and annealed denoising schedules in terms of reconstruction speed and accuracy. Experiments varied the initial denoising level $\sigma_{max} \in [0.02, 0.5]$ and the number of iterations K , while keeping other parameters fixed. Denoising schedules were logarithmically spaced and rounded to discrete Σ levels, with $\sigma_{max} = \sigma_{min} = 0.02$ corresponding to a fixed schedule. Table IV reports combined T1+T2 MAPE on representative *in-vivo* and BrainWeb volumes (in Figs 2 and S.1), while Fig. 7 shows the evolution of denoising levels σ_k and reconstruction errors over iterations ($K = 10/60$ for *in-vivo*/BrainWeb). Fixed denoising schedules show the slowest progress on reducing errors. Annealed schedules ($\sigma_{max} > 0.02$) enable faster reconstructions. For *in-vivo* data, $\sigma_{max} = 0.2$ achieved the lowest error using $K = 10$ iterations; larger K were sub-optimal in runtime and accuracy. The same σ_{max} performed best on BrainWeb, although its single-coil setting required more iterations due to poorer conditioning.

5) *Accuracy of CG updates*: We analyze runtime–accuracy trade-off of K_{cg} , the maximum number of CG iterations in the k-space-enforcing $prox_f$ updates (Algorithm 1, Line 10). Table V reports average per- $prox_f$ runtime and T1+T2 MAPE

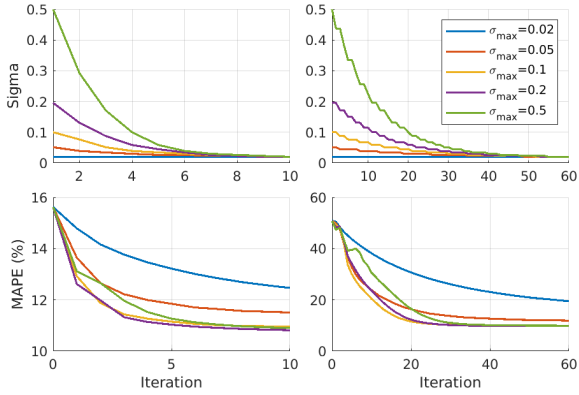


Fig. 7: MRI2Qmap denoising schedules σ_k (top) and T1+T2 MAPEs (bottom) vs. iterations for *in-vivo* (left) and BrainWeb (right) reconstruction examples.

σ_{\max}	<i>in-vivo</i> data					BrainWeb data				
	$K=5$	10	15	20	30	10	20	40	60	100
0.02	13.22	12.46	12.10	11.87	11.65	38.19	30.72	23.07	19.50	16.46
0.05	12.17	11.51	11.19	11.11	11.12	32.51	23.43	15.13	11.91	10.25
0.1	11.54	10.95	10.88	10.97	11.23	29.40	19.46	11.61	9.90	9.47
0.2	11.27	10.82	10.91	11.11	11.35	28.59	18.87	11.02	9.61	9.45
0.5	11.34	10.91	11.01	11.20	11.46	29.12	19.37	11.31	9.93	9.49

TABLE IV: Combined T1+T2 MAPE (%) across K , σ_{\max} on *in-vivo*/BrainWeb reconstruction examples.

K_{cg}	1	5	10	20	40
MAPE (%)	12.53	10.88	10.82	10.81	10.81
Avg./iter (s)	5.8	23.0	39.9	61.3	87.0

TABLE V: MRI2Qmap T1+T2 MAPE (%) and $prox_f$ average runtime (s) vs. CG iterations (K_{cg}) on an *in-vivo* volume.

errors on a representative *in-vivo* volume, with CG terminating at a relative residual of 10^{-5} or at K_{cg} . $K_{cg} \in [5, 10]$ provide a favorable trade-off: smaller values increased error, while larger ones yield only marginal gains ($\leq 0.01\%$) at higher runtime cost. Trends are similar on BrainWeb data (Supplementary Table S.1), overall indicating that depending on problem conditioning, CG updates require some moderate, but not high-precision convergence.

6) *Inexact dictionary matching*: Dictionary matching steps can be accelerated using approximate search methods [17], [18]. We evaluate Fast Group Matching (FGM), which clusters dictionary atoms by cosine similarity and restricts matching to a small subset of relevant groups, as detailed in [17]. In our experiments, FGM used 100 groups with cosine similarity thresholds of 0.95 (in vivo) and 0.98 (BrainWeb), chosen to balance accuracy and speed. Using FGM within MRI2Qmap produced nearly identical reconstructions (accuracy loss $\leq 0.07\%$ in combined T1+T2 MAPE), while achieving a 4–5.5 \times speedup in dictionary matching steps ($\sim 1.7s$ for BrainWeb and $\sim 2.4s$ for *in-vivo* data, down from $\sim 10s$ for exact matching).

7) *Other acquisition settings*: Finally, Table VI provides reconstruction results (zero-shot, without retraining the denoiser model) for *in-vivo* data on other acceleration factors $R = 2, 4, 6$, showing consistent performance of MRI2Qmap

Method	MAPE (%) \downarrow			PSNR (dB) \uparrow			
	T1+T2	T1	T2	T1w	T2w	PDw	
$R = 2$	LRTV	7.94	3.45	4.49	40.32	34.80	35.30
	MRFPnP	7.56	3.15	4.41	41.66	35.74	36.23
	MRI2Qmap	7.50	3.25	4.25	41.58	35.44	35.13
$R = 4$	LRTV	11.01	4.88	6.13	35.88	31.18	32.54
	MRFPnP	10.07	4.20	5.87	38.62	32.85	34.02
	MRI2Qmap	9.88	4.18	5.70	38.39	32.27	32.87
$R = 6$	LRTV	13.05	6.03	7.02	34.06	29.58	31.24
	MRFPnP	11.83	5.10	6.73	36.58	30.82	32.52
	MRI2Qmap	11.35	4.74	6.61	36.67	30.70	31.51

TABLE VI: MRI2Qmap performance vs. selected baselines on acceleration factors $R = 2, 4, 6$, averaged on *in-vivo* dataset.

across different acquisition settings. Results are compared with representative compressed-sensing and deep learning methods (LRTV, MRF-PnP); ARNet is excluded, since it requires retraining for each R . As R increases, errors rise for all methods, but deep learning approaches (MRI2Qmap, MRF-PnP) tend to remain more robust. MRI2Qmap achieves metrics comparable to supervised MRF-PnP despite no MRF training data (for qualitative comparisons see Fig S.4).

D. Limitations and future work

While the proposed framework shows promising results for MRF reconstruction, several extensions could further broaden its applicability. The current model reconstructs single-compartment, multi-parametric maps; future work could incorporate multi-compartment models to account for partial volume effects [51]. Motion artifacts are relevant in clinical applications and require the integration of motion-compensation modules [52]. Consistent with the preprocessing pipeline in [11], B0/B1 corrections were omitted; but these could be complementarily added to further improve quantitative accuracy [5]. Extensions to other qMRI sequences and bioparameters are also natural directions. From a computational perspective, further speedups are possible through stochastic optimization [53], improved preconditioning and multi-GPU parallelization [54]. Incorporating additional MRI contrasts (e.g. FLAIR) to further enrich multimodal priors, adopting more expressive denoising backbones [55], and possible integration with denoising diffusion models for probabilistic reconstruction [56] remain avenues for future investigation.

V. CONCLUSIONS

We show that image priors learned from independently acquired routine weighted-MRI datasets can support quantitative MRI reconstruction. We introduced MRI2Qmap, a plug-and-play framework based on deep denoising autoencoders pretrained on large multimodal MRI datasets. The method was validated on accelerated 3D whole-brain MRF data from *in vivo* and simulated acquisitions, achieving competitive or improved performance relative to MRF baselines without requiring ground-truth quantitative training data. Given the broad availability of routine MRI, this approach may enable more scalable, data-driven quantitative reconstruction using larger and more diverse datasets.

REFERENCES

- [1] P. Tofts, *Quantitative MRI of the brain: measuring changes caused by disease*. John Wiley & Sons, 2005.
- [2] D. Ma *et al.*, “Magnetic resonance fingerprinting,” *Nature*, vol. 495, no. 7440, pp. 187–192, 2013.
- [3] Y. Jiang *et al.*, “MR fingerprinting using fast imaging with steady state precession (FISP) with spiral readout,” *Magn Reson Med*, vol. 74, no. 6, pp. 1621–1631, 2015.
- [4] P. Gómez *et al.*, “Rapid three-dimensional multiparametric mri with quantitative transient-state imaging,” *Scientific reports*, vol. 10, no. 1, p. 13769, 2020.
- [5] X. Cao *et al.*, “Optimized multi-axis spiral projection MR fingerprinting with subspace reconstruction for rapid whole-brain high-isotropic-resolution quantitative imaging,” *Magn Reson Med*, vol. 88, no. 1, pp. 133–150, 2022.
- [6] J. Assländer *et al.*, “Low rank alternating direction method of multipliers reconstruction for MR fingerprinting,” *Magn Reson Med*, vol. 79, no. 1, pp. 83–96, 2018.
- [7] G. Mazor, L. Weizman, A. Tal, and Y. Eldar, “Low-rank magnetic resonance fingerprinting,” *Med. Phys.*, vol. 45, no. 9, pp. 466–484, 2018.
- [8] M. Golbabaee *et al.*, “Compressive mri quantification using convex spatiotemporal priors and deep encoder-decoder networks,” *Med. Image Anal.*, vol. 69, p. 101945, 2021.
- [9] Z. Fang *et al.*, “Deep learning for fast and spatially constrained tissue quantification from highly accelerated data in magnetic resonance fingerprinting,” *IEEE Trans. Med. Imag.*, vol. 38, pp. 2364–2374, 2019.
- [10] P. Li and Y. Hu, “Learned tensor low-rp-rank and bloch response manifold priors for non-cartesian mrf reconstruction,” *IEEE Trans. Med. Imag.*, vol. 42, no. 12, pp. 3702–3714, 2023.
- [11] S. S. Schauman *et al.*, “Deep learning initialized compressed sensing (deli-cs) in volumetric spatio-temporal subspace reconstruction,” *Magn Reson Mater Phys*, vol. 38, no. 2, pp. 221–237, 2025.
- [12] P. Mayo, C. M. Pirkil, A. Achim, B. Menze, and M. Golbabaee, “Physics informed guided diffusion for accelerated multi-parametric MRI reconstruction,” in *MICCAI*. Springer Nature Switzerland, 2025.
- [13] J. Warntjes, O. D. Leinhard, J. West, and P. Lundberg, “Rapid magnetic resonance quantification on the brain: optimization for clinical usage,” *Magn Reson Med*, vol. 60, no. 2, pp. 320–329, 2008.
- [14] V. Gulani *et al.*, “Towards a single-sequence neurologic magnetic resonance imaging examination: multiple-contrast images from an IR TrueFISP experiment,” *Invest. Radiol.*, vol. 39, no. 12, 2004.
- [15] D. McGivney *et al.*, “SVD compression for magnetic resonance fingerprinting in the time domain,” *IEEE Trans. Med. Imag.*, vol. 33, no. 12, pp. 2311–2322, 2014.
- [16] M. Davies, G. Puy, P. Vandergheynst, and Y. Wiaux, “A compressed sensing framework for magnetic resonance fingerprinting,” *SIAM J. Imag. Sci.*, vol. 7, no. 4, pp. 2623–2656, 2014.
- [17] S. Cauley *et al.*, “Fast group matching for MR fingerprinting reconstruction,” *Magn Reson Med*, vol. 74, no. 2, pp. 523–528, 2015.
- [18] M. Golbabaee, Z. Chen, Y. Wiaux, and M. Davies, “CoverBLIP: accelerated and scalable iterative matched-filtering for magnetic resonance fingerprint reconstruction,” *Inverse Problems*, vol. 36, p. 015003, 2019.
- [19] B. Zhao *et al.*, “Improved magnetic resonance fingerprinting reconstruction with low-rank and subspace modeling,” *Magn Reson Med*, vol. 79, no. 2, pp. 933–942, 2018.
- [20] B. Zhao, B. Bilgic *et al.*, “Simultaneous multislice magnetic resonance fingerprinting with low-rank and subspace modeling,” in *IEEE Engineering in Medicine and Biology Society*. IEEE, 2017, pp. 3264–3268.
- [21] G. Cruz *et al.*, “Sparsity and locally low rank regularization for MR fingerprinting,” *Magn Reson Med*, vol. 81, no. 6, pp. 3530–3543, 2019.
- [22] E. Hoppe *et al.*, “Deep learning for magnetic resonance fingerprinting: a new approach for predicting quantitative parameter values from time series,” in *German Medical Data Sciences*, 2017, pp. 202–206.
- [23] O. Cohen, B. Zhu, and M. S. Rosen, “MR fingerprinting deep reconstruction network (DRONE),” *Magn Reson Med*, vol. 80, no. 3, pp. 885–894, 2018.
- [24] M. Golbabaee *et al.*, “Geometry of deep learning for magnetic resonance fingerprinting,” in *IEEE ICASSP*, 2019, pp. 7825–7829.
- [25] R. Soyak *et al.*, “Channel attention networks for robust MR fingerprint matching,” *IEEE Trans. Biomed. Eng.*, vol. 69, pp. 1398–1405, 2021.
- [26] F. Cheng, Y. Liu, Y. Chen, and P.-T. Yap, “High-resolution 3d magnetic resonance fingerprinting with a graph convolutional network,” *IEEE Trans. Medical Imag.*, vol. 42, no. 3, pp. 674–683, 2022.
- [27] D. Chen, M. E. Davies, and M. Golbabaee, “Compressive mr fingerprinting reconstruction with neural proximal gradient iterations,” in *MICCAI*. Springer, 2020, pp. 13–22.
- [28] K. Fatania *et al.*, “A plug-and-play approach to multiparametric quantitative MRI: image reconstruction using pre-trained deep denoisers,” in *IEEE Int. Symp. Biomed. Imaging*, 2022, pp. 1–4.
- [29] P. Li and Y. Hu, “Deep magnetic resonance fingerprinting based on local and global vision transformer,” *Med. Image Anal.*, vol. 95, 2024.
- [30] W. Bian, A. Jang, and F. Liu, “Improving quantitative mri using self-supervised deep learning with model reinforcement: demonstration for rapid t1 mapping,” *Magn Reson Med*, vol. 92, no. 1, pp. 98–111, 2024.
- [31] Y. Jun *et al.*, “Zero-deepsup: zero-shot deep subspace reconstruction for rapid multiparametric quantitative mri using 3d-qalms,” *Magn Reson Med*, vol. 91, no. 6, pp. 2459–2482, 2024.
- [32] J. Hamilton, “A self-supervised deep learning reconstruction for shortening the breathhold and acquisition window in cardiac magnetic resonance fingerprinting,” *Front. Cardiovasc. Med.*, vol. 9, p. 928546, 2022.
- [33] P. Mayo *et al.*, “Deep image priors for magnetic resonance fingerprinting with pretrained bloch-consistent denoising autoencoders,” in *IEEE Int. Symp. Biomed. Imaging*, 2024, pp. 1–4.
- [34] D. Chen, J. Tachella, and M. E. Davies, “Equivariant imaging: Learning beyond the range space,” in *IEEE/CVF Int. Conf. Computer Vision*, 2021, pp. 4379–4388.
- [35] P. Vincent, “A connection between score matching and denoising autoencoders,” *Neural computation*, vol. 23, no. 7, pp. 1661–1674, 2011.
- [36] R. Ahmad *et al.*, “Plug-and-play methods for magnetic resonance imaging: Using denoisers for image recovery,” *IEEE Signal Process. Mag.*, vol. 37, no. 1, pp. 105–116, 2020.
- [37] K. Zhang *et al.*, “Plug-and-play image restoration with deep denoiser prior,” *IEEE Trans. Pattern Anal. Mach. Intell.*, vol. 44, no. 10, pp. 6360–6376, 2021.
- [38] U. Kamilov, C. Bouman, G. Buzzard, and B. Wohlberg, “Plug-and-play methods for integrating physical and learned models in computational imaging: Theory, algorithms, and applications,” *IEEE Signal Process. Mag.*, vol. 40, no. 1, pp. 85–97, 2023.
- [39] S. Boyd *et al.*, “Distributed optimization and statistical learning via the alternating direction method of multipliers,” *Found. Trends Mach. Learn.*, vol. 3, no. 1, pp. 1–122, 2011.
- [40] S. Venkatakrishnan, C. Bouman, and B. Wohlberg, “Plug-and-play priors for model based reconstruction,” in *IEEE GlobalSIP*, 2013, pp. 945–948.
- [41] P. Dhariwal and A. Nichol, “Diffusion models beat GANs on image synthesis,” *Adv Neural Inf Process Syst*, vol. 34, pp. 8780–8794, 2021.
- [42] V. Essen *et al.*, “The WU-Minn human connectome project: an overview,” *Neuroimage*, vol. 80, pp. 62–79, 2013.
- [43] “IXI Dataset,” <https://brain-development.org/ixi-dataset/>.
- [44] “Project MONAI,” <https://github.com/Project-MONAI>.
- [45] C. Baron, N. Dwork, J. Pauly, and D. Nishimura, “Rapid compressed sensing reconstruction of 3d non-cartesian mri,” *Magn Reson Med*, vol. 79, no. 5, pp. 2685–2692, 2018.
- [46] J. Tamir *et al.*, “T2 shuffling: sharp, multicontrast, volumetric fast spin-echo imaging,” *Magn Reson Med*, vol. 77, no. 1, pp. 180–195, 2017.
- [47] M. Cencini *et al.*, “MRTwin: an open-source Python package to create virtual qMRI phantoms for benchmark and synthetic data generation,” in *Int Soc Magn Reson Med*, 2025.
- [48] D. Collins *et al.*, “Design and construction of a realistic digital brain phantom,” *IEEE Trans. Med. Imag.*, vol. 17, no. 3, pp. 463–468, 2002.
- [49] A. Beck and M. Teboulle, “A fast iterative shrinkage-thresholding algorithm for linear inverse problems,” *SIAM J. Imag. Sci.*, vol. 2, no. 1, pp. 183–202, 2009.
- [50] B. Billot *et al.*, “Synthseg: Segmentation of brain mri scans of any contrast and resolution without retraining,” *Med. Image Anal.*, vol. 86, p. 102789, 2023.
- [51] D. McGivney *et al.*, “Bayesian estimation of multicomponent relaxation parameters in magnetic resonance fingerprinting,” *Magn Reson Med*, vol. 80, no. 1, pp. 159–170, 2018.
- [52] G. Cruz *et al.*, “Generalized low-rank nonrigid motion-corrected reconstruction for mr fingerprinting,” *Magn Reson Med*, vol. 87, no. 2, 2022.
- [53] P. Mayo *et al.*, “Stodip: Efficient 3d mrf image reconstruction with deep image priors and stochastic iterations,” in *International Workshop on Machine Learning in Medical Imaging*. Springer, 2024, pp. 128–137.
- [54] S. Iyer *et al.*, “Polynomial preconditioners for regularized linear inverse problems,” *SIAM J. Imag. Sci.*, vol. 17, no. 1, pp. 116–146, 2024.
- [55] Q. Shou *et al.*, “Transformer-based deep learning denoising of single and multi-delay 3d arterial spin labeling,” *Magn Reson Med*, vol. 91, no. 2, pp. 803–818, 2024.
- [56] G. Luo, M. Blumenthal, M. Heide, and M. Uecker, “Bayesian mri reconstruction with joint uncertainty estimation using diffusion models,” *Magn Reson Med*, vol. 90, no. 1, pp. 295–311, 2023.

MRI2QMAP: SUPPLEMENTARY MATERIALS

S.I. PROOF OF EXPRESSIONS (10) AND (11)

Dictionary matching is performed independently at each voxel; for brevity, we omit the voxel index. Let $\tilde{\mathbf{x}} \in \mathbb{C}^s$ and $\tilde{\mathbf{m}} \in \mathbb{R}_+^{s'}$ denote the signals of a voxel from a s -channel TSMI and a stack of s' -channel MRI modalities, respectively. Let $D_j^{\mathcal{Q}} \in \mathbb{C}^s$ and $D_j^{\mathcal{W}} \in \mathbb{R}_+^{s'}$ respectively denote atoms of the MRF and MRI dictionaries indexed by $j \in \text{LUT}$ indicating a certain tissue property. The combined MRF-MRI dictionary matching is defined as:

$$\operatorname{argmin}_{j \in \text{LUT}, \text{PD} \in \mathbb{C}} \|\tilde{\mathbf{x}} - \text{PD} \cdot D_j^{\mathcal{Q}}\|_2^2 + \|\tilde{\mathbf{m}} - |\text{PD}| \cdot D_j^{\mathcal{W}}\|_{\gamma}^2, \quad (\text{S.1})$$

or equivalently,

$$\operatorname{argmin}_{j \in \text{LUT}, \text{PD} \in \mathbb{C}} |\text{PD}|^2 A_j - 2\operatorname{Re}\langle \tilde{\mathbf{x}}, \text{PD} D_j^{\mathcal{Q}} \rangle - 2\langle \tilde{\mathbf{m}}, |\text{PD}| D_j^{\mathcal{W}} \rangle_{\gamma} \quad (\text{S.2})$$

where $A_j := \|D_j^{\mathcal{Q}}\|_2^2 + \|D_j^{\mathcal{W}}\|_{\gamma}^2$. The objective of (S.2) depends on the PD's phase (denoted by \angle) only in its second term, and is minimized by setting the optimal phase $\angle \text{PD}^* = -\angle \langle \tilde{\mathbf{x}}, D_j^{\mathcal{Q}} \rangle$ or equivalently:

$$\angle \text{PD}^* = \angle \langle D_j^{\mathcal{Q}}, \tilde{\mathbf{x}} \rangle = \frac{\langle D_j^{\mathcal{Q}}, \tilde{\mathbf{x}} \rangle}{|\langle D_j^{\mathcal{Q}}, \tilde{\mathbf{x}} \rangle|}. \quad (\text{S.3})$$

Substituting (S.3) in the objective of (S.2) gives:

$$|\text{PD}|^2 A_j - 2|\text{PD}| B_j, \quad (\text{S.4})$$

where $B_j := |\langle \tilde{\mathbf{x}}, D_j^{\mathcal{Q}} \rangle| + \langle \tilde{\mathbf{m}}, D_j^{\mathcal{W}} \rangle_{\gamma} > 0$. The minimizing PD magnitude is therefore:

$$|\text{PD}^*| = B_j / A_j. \quad (\text{S.5})$$

Together, the optimal phase and magnitude prove the closed-form expression (11). Substituting (S.5) in (S.4) yields $-B_j^2/A_j$ as for the objective of (S.2), which is minimized by searching over LUT the j^* that maximizes $B_j/\sqrt{A_j}$ as in (10), which completes the proof.

S.II. SIMULATED BRAINWEB DATASET

The simulated dataset was generated using 3D quantitative T1, T2, and PD maps produced with the MRTwin software [47] from anatomical brain models in the BrainWeb database [48]. BrainWeb provides 20 normal-brain models at 0.5 mm isotropic resolution; these were resampled to 1 mm³ isotropic resolution and cropped to a 256³-voxel volume. MRTwin constructed quantitative maps using BrainWeb's fuzzy tissue-segmentation maps and their assigned (T_1 ms, T_2 ms, PD au) properties for the following tissue classes: Background/skull (0, 0, 0), Cerebrospinal fluid (4000, 1990, 1), Gray matter (1250, 90, 85), White matter (750, 70, 75), Fat (250, 70, 1), Muscle/skin (1485, 50, 1), Vessels (1960, 200, 1.5), Around fat (250, 70, 1), Dura matter (990, 150, 1), Bone marrow (587, 50, 1). For evaluation, binary tissue masks were derived from the ground-truth fuzzy segmentation maps by thresholding tissue probabilities at 90%.

S.III. IMPLEMENTATION DETAILS

Baselines methods: **LLR** [5] and **LRTV** [8] are convex reconstruction methods that enforce k-space consistency with TSMI regularization based on locally low-rank and total variation priors, respectively. The regularization strength parameters λ was set to $\lambda = 3\text{e-}6/5\text{e-}7$ for LLR and $\lambda = 2\text{e-}7/4\text{e-}8$ for LRTV in *in-vivo*/BrainWeb experiments. Both methods employ FISTA, using 60 iterations for *in-vivo* data (multicoil, better conditioned, faster convergence) and 500 iterations for single-coil BrainWeb data (slower convergence). For LRTV, *prox_R* used the Chambolle-Pock algorithm, while LLR employed singular-value soft-thresholding over non-overlapping TSMI patches (spatial size 8³) from the toolbox in [11]. GPU acceleration was used for both proximal operators.

ARNet used the same U-Net backbone as MRI2Qmap denoiser, with input/output channel dimensions modified for TSMI restoration (10 channels for both input and output, representing the stack of real and imaginary components of the $s = 5$ complex-valued TSMI channels). The class- and noise-level conditioning were not applicable and therefore disabled. Training used paired MRF data. Inputs (\mathbf{x}_{init}) were CG-reconstructed TSMI from $R = 8$ accelerated acquisitions (the same initialization used in MRI2Qmap reconstruction), and targets were reference TSMIs generated either from ground-truth qmaps in BrainWeb experiment, or from qmaps obtained from the gold-standard $R = 1$ acquisitions for *in-vivo* dataset. All TSMI volumes were normalized to $[-1, 1]$. The network was trained using MSE loss on randomly cropped input-target patches (spatial size 64³), with random intensity scaling (up to $\pm 50\%$) for augmentation, using Adam optimizer, learning rate 10^{-4} , batch size 5, and 10k training epochs. During inference, ARNet was used to restore CG-reconstructed TSMI patches (overlapping patches of stride size 32 was used).

MRF-PnP [29] is an ADMM-based plug-and-play algorithm for TSMI reconstruction $\min_{\mathbf{x}} f(\mathbf{x}) + \mathcal{R}(\mathbf{x})$ based on enforcing k-space data fidelity and a data-driven TSMI Gaussian DAE prior replacing the regularizer's proximal step. Unlike MRI2Qmap, the DAE directly restores MRF time-frame data; training therefore required high-quality TSMIs, obtained from ground-truth qmaps (BrainWeb experiment) or from long, densely sampled $R = 1$ MRF acquisitions (*in-vivo* experiment). The TSMI denoiser employed the same UNet architecture as MRI2Qmap, with 10-channel TSMI input/output formed by stacking real and imaginary components. For training, TSMIs were normalized to $[-1, 1]$, randomly cropped into patches (spatial size 64³), random intensity scaling (up to $\pm 50\%$), and corrupted with additive Gaussian noise at experimentally selected standard deviations $\sigma \in \{0.1, 0.05, 0.025, 0.01\}$ using noise-level conditioning; class conditioning was disabled. Models were trained with MSE loss and Adam optimization (learning rate 10^{-4} , batch size 5) for 10k epochs. Reconstruction from $R = 8$ acquisitions was initialized with CG-reconstructed TSMI \mathbf{x}_{init} as in MRI2Qmap, and alternated CG-based *prox_f* updates with TSMI denoising (random-shifts augmentation and non-overlapped patch denoising, like MRI2Qmap). Reconstruction parameters were $K = K_{c_g} = 10$, $\sigma = 0.025$, $\mu = 10^{-5}$ for

in-vivo data and $K = 60$, $K_{cg} = 20$, $\sigma = 0.05$, $\mu = 5 \times 10^{-6}$ for BrainWeb, where K and K_{cg} denote the PnP and inner CG iterations, respectively. The denoising level σ and the ADMM penalty μ parameters were kept fixed during iterations following [29] with values searched to yield best quantitative mapping performance.

S.IV. ADDITIONAL EXPERIMENTAL RESULTS

A. Reconstructed maps from BrainWeb experiment

The supplementary Fig. S.1 presents reconstructed T1/T2 maps from MRI2Qmap and baseline methods for a representative BrainWeb test volume at an acquisition acceleration factor of $R = 8$, together with corresponding percentage error maps relative to the ground-truth reference. The MRF-ADMM baseline without spatial regularization exhibits pronounced aliasing artifacts. Incorporating spatial regularization via LLR/LRTV improves reconstruction quality; however, these methods generally incur higher errors than deep learning baselines (ARNet, MRF-PnP, and MRI2Qmap) due to residual aliasing and/or over-smoothing. MRI2Qmap shows the lowest errors, comparable to the best-performing supervised MRF-domain baseline (MRF-PnP), despite not being trained on MRF data.

B. Reconstructed maps from other *in-vivo* subjects

The supplementary Figs. S.2 and S.3 show the axial and coronal views, respectively, of the reconstructed *in-vivo* T1/T2

maps at acceleration factor $R = 8$. Results are shown for MRI2Qmap and representative compressed-sensing and deep-learning baselines (LRTV and ARNet) for the remaining *in-vivo* subjects not included in the main manuscript figures.

C. Accuracy of CG updates: BrainWeb experiment

To complement the *in-vivo* analysis in Table V, we provide the runtime–accuracy analysis of the maximum number of CG iterations (K_{cg}) in the $prox_f$ updates for simulated single-coil BrainWeb reconstructions. Table S.1 reports average per- $prox_f$ runtime and the final T1+T2 MAPE reconstruction errors for a representative BrainWeb volume (in Fig. S.1), with CG stopping at a relative residual of 10^{-5} or at the iteration limit K_{cg} . The base-model choice $K_{cg} = 20$ for BrainWeb experiments provides a favorable trade-off in runtime-accuracy: smaller K_{cg} increases errors, while larger values give relatively small accuracy gains despite higher runtime cost. We also note that poorer conditioning of single-coil reconstructions necessitates larger K_{cg} in the $prox_f$ step for BrainWeb than for *in-vivo* data, although each CG iteration is faster than in multicoil *in-vivo* reconstructions.

K_{cg}	5	10	20	40	60
MAPE (%)	20.18	11.67	9.61	9.49	9.49
Avg./iter (s)	2.5	4.5	8.4	14.4	18.1

TABLE S.1: MRI2Qmap T1+T2 MAPE (%) and $prox_f$ average runtime (s) vs. CG iterations (K_{cg}) on BrainWeb data.

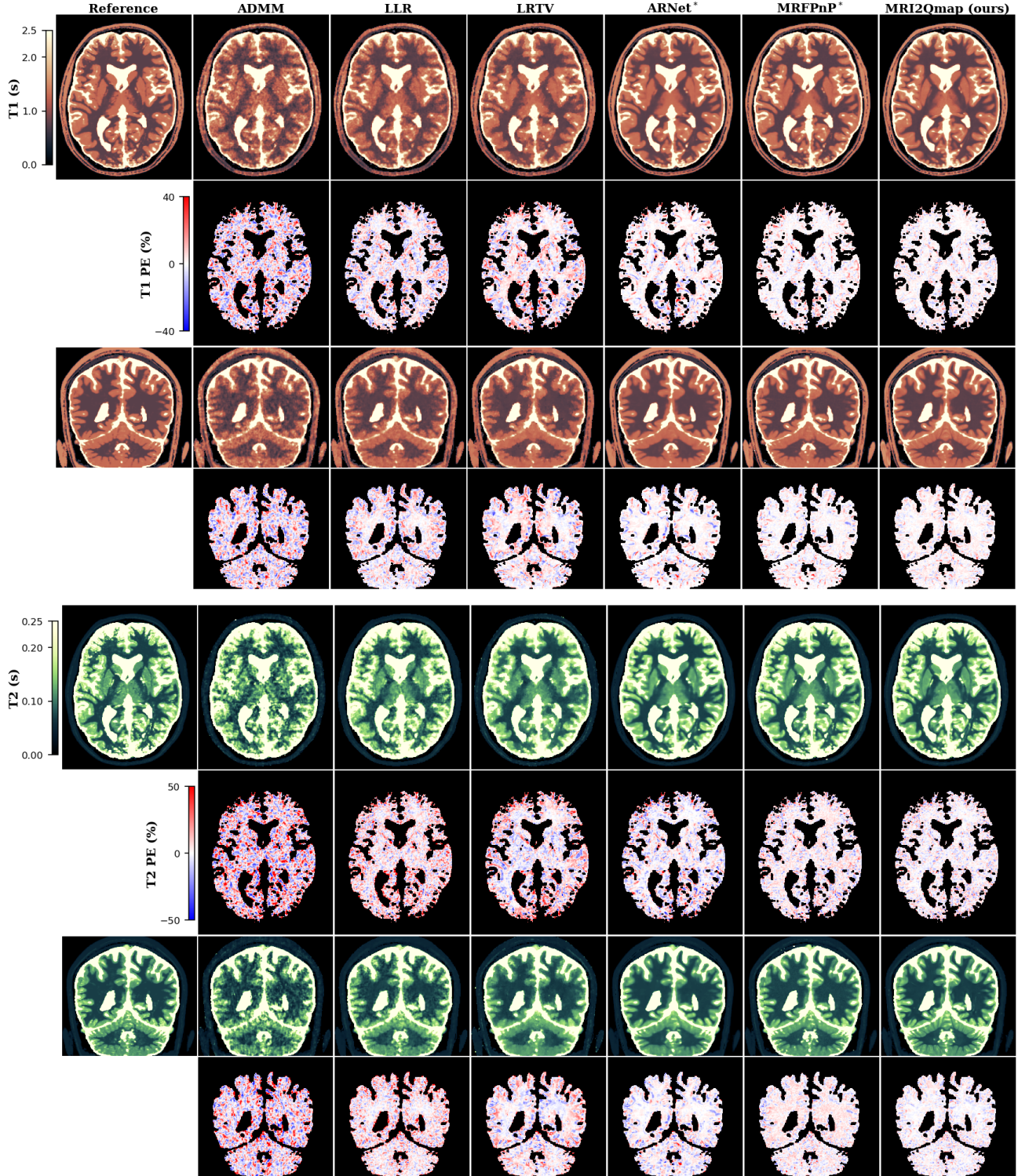


Fig. S.1: Reconstructed T1/T2 maps (axial and coronal views) at acceleration factor $R = 8$ for a representative simulated BrainWeb subject, comparing MRI2Qmap with MRF baselines (* indicates MRF-trained methods). Percentage error (PE) maps relative to the ground-truth reference are shown below each reconstruction.

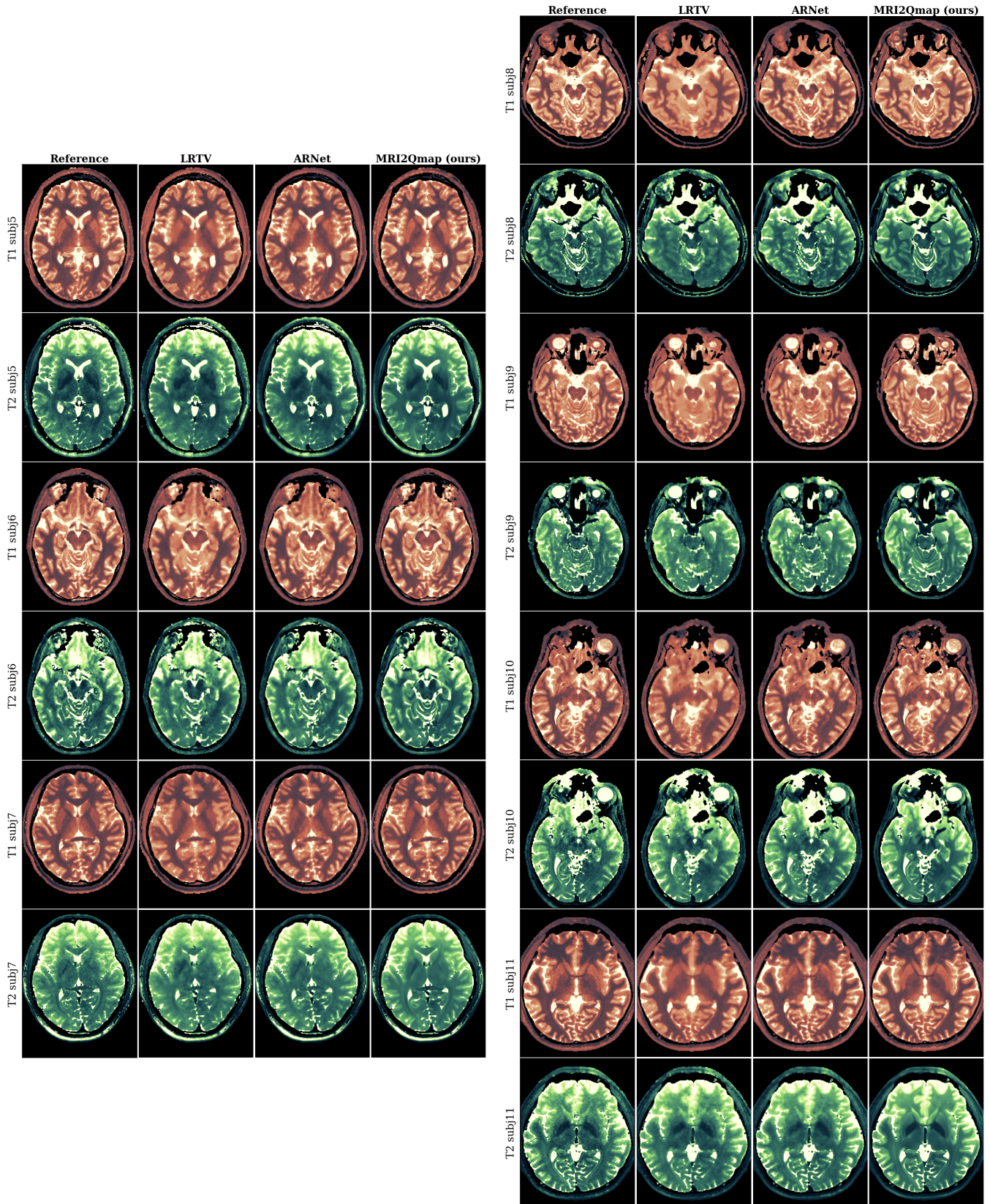


Fig. S.2: Reconstructed T1 and T2 maps (axial view) at $R = 8$ for the remaining seven subjects in *in-vivo* dataset, comparing MRI2Qmap with representative baselines (LRTV and ARNet). Relative to baselines, MRI2Qmap exhibits reduced artifacts and improved anatomical delineation (electronic zooming recommended).

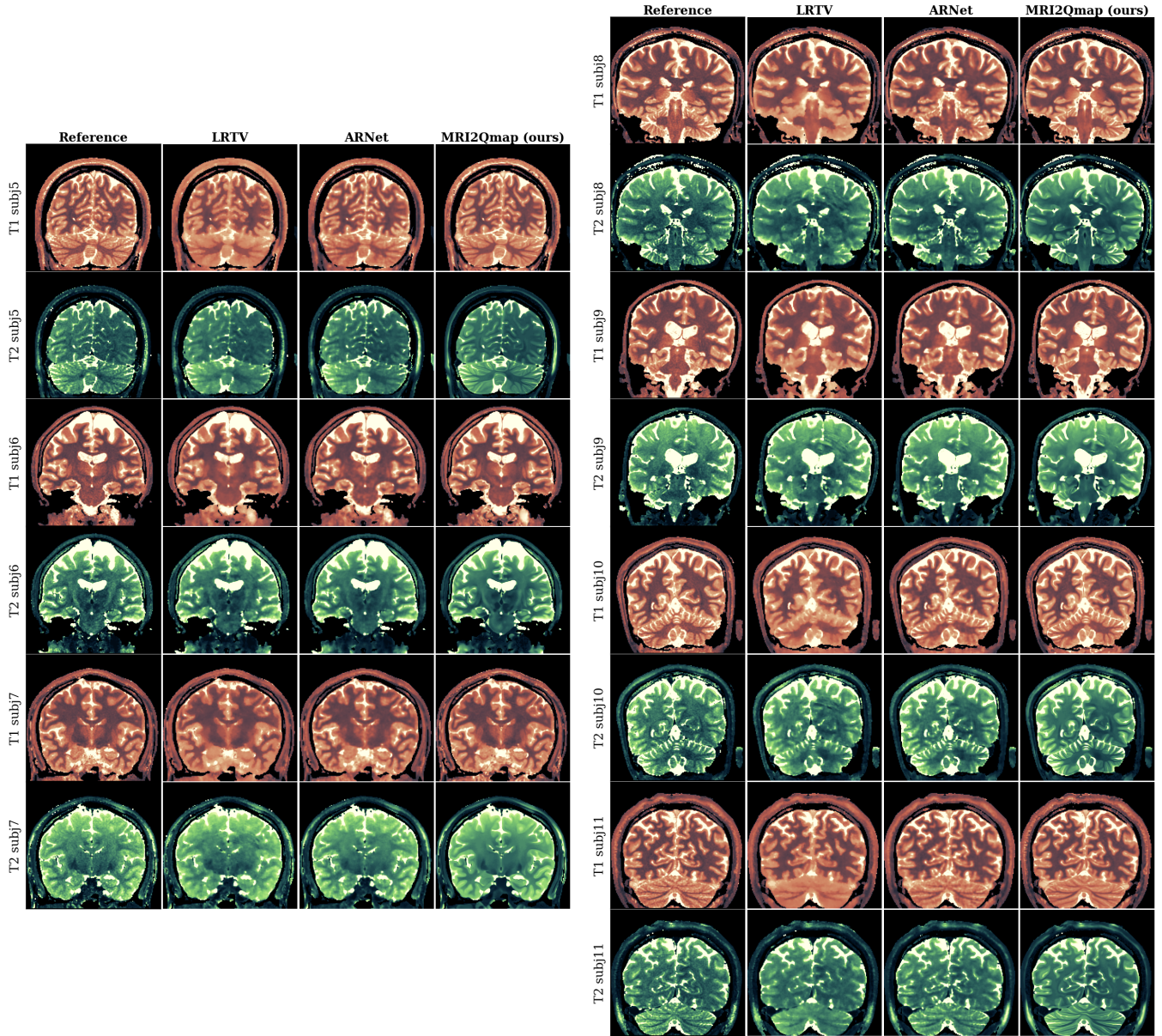


Fig. S.3: Reconstructed T1 and T2 maps (coronal view) at $R = 8$ for the remaining seven subjects in *in-vivo* dataset, comparing MRI2Qmap with representative baselines (LRTV and ARNet). Relative to baselines, MRI2Qmap exhibits reduced artifacts and improved anatomical delineation (electronic zooming recommended).

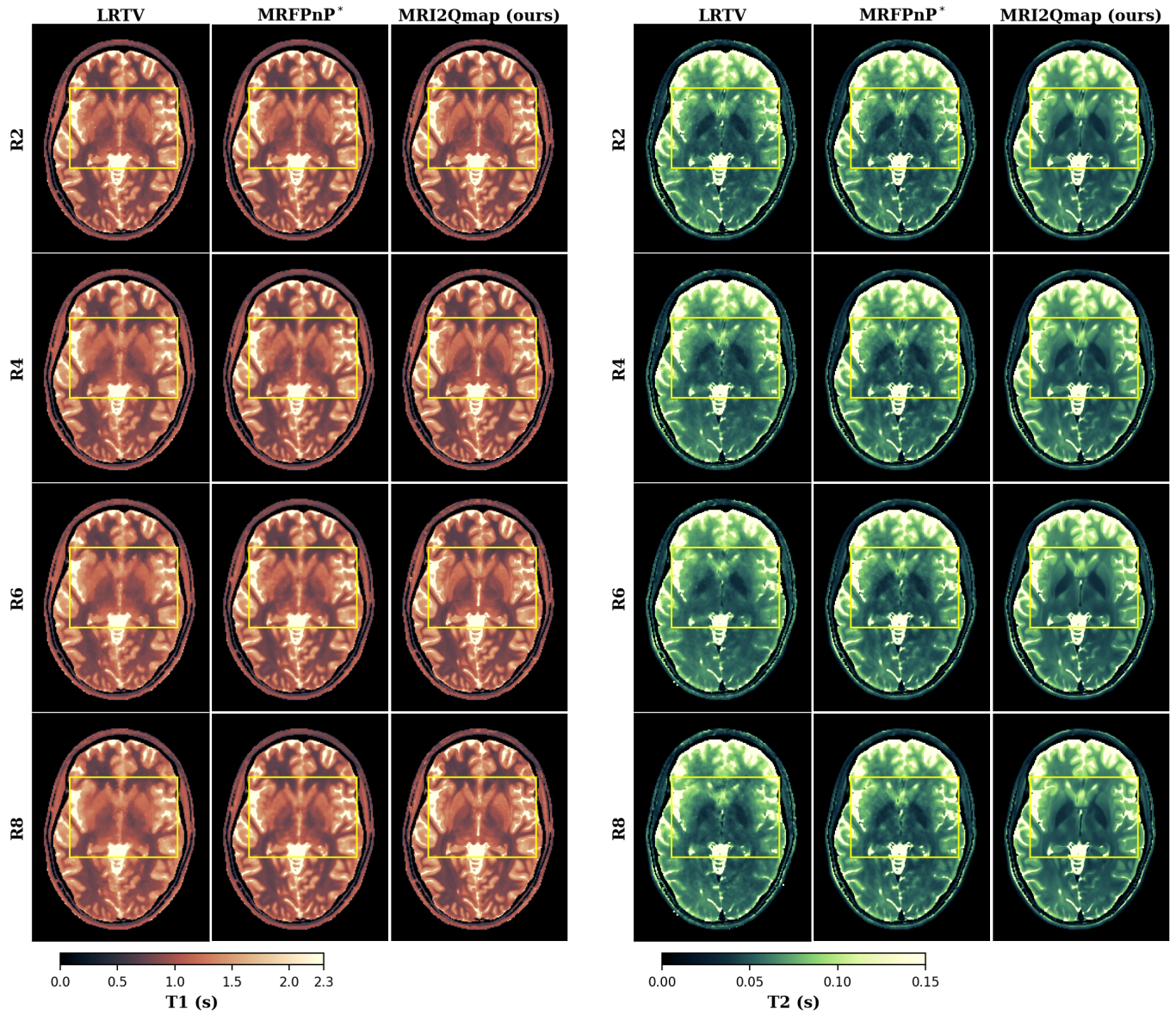


Fig. S.4: Reconstructed T1 and T2 maps at acquisition acceleration factors $R = 2, 4, 6, 8$ (rows) for a representative *in-vivo* test image. Relative to baselines (*indicates MRF-trained), MRI2Qmap exhibits reduced artifacts and improved delineation of deep brain structures (electronic zoom in boxed regions is recommended).